

1 **Host Cell Proteases Drive Early or Late SARS-CoV-2 Penetration**

2 Jana Koch^{1,2,3,#}, Zina M Uckley^{1,2,3,#}, Patricio Doldan^{1,3}, Megan Stanifer^{1,5,*}, Steeve Boulant^{1,3,4,*},

3 Pierre-Yves Lozach^{1,2,3,6,*}

4 ¹Center for Integrative Infectious Diseases Research (CIID), University Hospital Heidelberg,

5 69120 Heidelberg, Germany; ²CellNetworks – Cluster of Excellence, 69120 Heidelberg, Germany;

6 ³Department of Infectious Diseases, Virology, University Hospital Heidelberg, 69120 Heidelberg,

7 Germany; ⁴German Cancer Center (DKFZ), 69120 Heidelberg, Germany; ⁵Department of

8 Infectious Diseases, Molecular Virology, University Hospital Heidelberg, 69120 Heidelberg,

9 Germany; ⁶Univ. Lyon, INRAE, EPHE, IVPC, 69007 Lyon, France

10 [#]these authors contributed equally

11 *Correspondence: pierre-yves.lozach@med.uni-heidelberg.de; m.stanifer@dkfz-heidelberg.de;

12 s.boulant@dkfz-heidelberg.de

13 Running title: SARS-CoV-2 entry

14 **Keywords**

15 Coronavirus; COVID-19; protease; SARS-CoV-2; virus entry

16 **Author contributions**

17 J.K., Z.M.U., and P.Y.L. designed research; J.K., Z.M.U., P.D., and M.S. performed research; J.K.,

18 Z.M.U., M.S., S.B., and P.Y.L. analyzed data; P.Y.L. wrote the original draft; and J.K., Z.M.U.,

19 M.S., S.B., and P.Y.L. reviewed and edited the paper.

20 The authors declare no conflict of interest.

21 **Abstract**

22 SARS-CoV-2 is a newly emerged coronavirus (CoV) that spread through human populations
23 worldwide in early 2020. CoVs rely on host cell proteases for activation and infection. The trypsin-
24 like protease TMPRSS2 at the cell surface, cathepsin L in endolysosomes, and furin in the Golgi
25 have all been implicated in the SARS-CoV-2 proteolytic processing. Whether SARS-CoV-2
26 depends on endocytosis internalization and vacuolar acidification for infectious entry remains
27 unclear. Here, we examined the dynamics of SARS-CoV-2 activation during the cell entry process
28 in tissue culture. Using four cell lines representative of lung, colon, and kidney epithelial tissues,
29 we found that TMPRSS2 determines the SARS-CoV-2 entry pathways. In TMPRSS2-positive
30 cells, infection was sensitive to aprotinin, a TMPRSS2 inhibitor, but not to SB412515, a drug that
31 impairs cathepsin L. Infectious penetration was marginally dependent on endosomal acidification,
32 and the virus passed the protease-sensitive step within 10 min. In a marked contrast, in
33 TMPRSS2-negative cells cathepsin L and low pH were required for SARS-CoV-2 entry. The
34 cathepsin L-activated penetration occurred within 40-60 min after internalization and required
35 intact endolysosomal functions. Importantly, pre-activation of the virus allowed it to bypass the
36 need for endosomal acidification for viral fusion and productive entry. Overall, our results indicate
37 that SARS-CoV-2 shares with other CoVs a strategy of differential use of host cell proteases for
38 activation and infectious penetration. This study also highlights the importance of TMPRSS2 in
39 dictating the entry pathway used by SARS-CoV-2.

40 **Significance**

41 Preventing SARS-CoV-2 spread requires approaches affecting early virus-host cell interactions
42 before the virus enters and infects target cells. Host cell proteases are critical for coronavirus
43 activation and infectious entry. Here, we reconcile apparent contradictory observations from
44 recent reports on endosomal acidification and the role of furin, TMPRSS2, and cathepsin L in the
45 productive entry and fusion process of SARS-CoV-2. Investigating authentic virus in various cell

46 types, we demonstrated that SARS-CoV-2 developed the ability to use different entry pathways,
47 depending on the proteases expressed by the target cell. Our results have strong implications for
48 future research on the apparent broad tropism of the virus *in vivo*. This study also provides a
49 handle to develop novel antiviral strategies aiming to block virus entry, as illustrated with the
50 several drugs that we identified to prevent SARS-CoV-2 infection, some with low IC₅₀.

51 **Introduction**

52 The *Coronaviridae* is a large viral family of several hundred members, which constitutes along
53 with *Arteriviridae* and *Roniviridae* the order *Nidovirales* (1). To date, four coronaviruses (CoVs)
54 have been identified as the leading cause for common colds in humans (2). Three other CoVs,
55 causing severe respiratory diseases, have emerged into the human population as a result of
56 spillover events from wildlife during the last two decades (3). Severe acute respiratory syndrome
57 (SARS)-CoV and Middle East respiratory syndrome (MERS)-CoV were first isolated in China in
58 2002 and Saudi Arabia in 2011, respectively (3). The most recent, SARS-CoV-2, is responsible
59 for CoV induced disease (COVID-19) and turned into a pandemic in early 2020. As of December
60 22, 2020, more than 77 million human cases have been reported with at least 1.7 million deaths.

61 As other CoVs, SARS-CoV-2 particles are enveloped, roughly spherical, with a diameter
62 between 90 and 110 nm (4, 5). The viral genome consists of one single-stranded positive-sense
63 RNA segment that replicates in the cytosol and encodes four structural proteins. Three
64 transmembrane proteins are embedded in the viral envelope and are exposed at the virion
65 surface, namely the large glycoprotein S, the membrane protein M, and the envelope protein E
66 (3). The nucleoprotein NP binds to the genomic RNA to form nucleocapsid structures inside the
67 viral particles. In the viral envelope, glycoprotein S forms spike-like projections up to 35 nm in
68 length, responsible for virus attachment to host cells and penetration by membrane fusion (6).

69 Although SARS-CoV-2 has been the subject of intense research since the beginning of
70 2020, our current understanding of cell entry remains essentially derived from studies on SARS-
71 CoV and other CoVs (3). SARS-CoV-2 has been shown to rely on ACE2 (7), heparan sulfates (8),
72 and neuropilin-1 (9) at the cell surface for infection. Inhibitor studies support the possibility that the
73 virus enters the endosomal vesicles and relies on vacuolar acidification for the infectious entry
74 process (7, 10, 11). As with many other CoVs, there is intense debate as to whether SARS-CoV-
75 2 enters the host cells from the plasma membrane or from intracellular compartments.

76 To gain access into the cytosol, enveloped viruses must fuse their envelope with the cell
77 membrane. Several classes of viral fusion proteins are known to mediate this process, each with
78 their own molecular specificities [reviewed in (12)]. Structural studies categorized the SARS-CoV-
79 2 protein S as a Class-I viral fusion protein, within the same group as other corona-, human
80 immunodeficiency, and influenza (IAV) viruses (13-15). Cryo-electron microscopy showed that the
81 S protein forms homotrimers at the surface of SARS-CoV-2 particles, in which the viral fusion
82 subunits are buried (13, 14). The activation of the Class-I viral fusion proteins usually involves
83 proteolytic processing, and membrane fusion is triggered by interactions with cell receptors and
84 sometimes endosomal acidification. Activation and priming are irreversible steps, and the Class-I
85 viral fusion proteins act only once (12). In the case of SARS-CoV-2, endosomal acidification
86 appears to be non-essential to induce the spike-mediated fusion of the host membrane with the
87 viral envelope (16). Yet why SARS-CoV-2 infection is sensitive to perturbants of endosomal
88 acidification remains unclear.

89 Several proteases have been proposed to prime and activate the S protein (17), a step prior
90 virus fusion and infection. Furin is a calcium-dependent serine endoprotease widely expressed in
91 tissues. It has been proposed to cleave the S protein at the site S1/S2 (17-19), most likely when
92 the viral progeny exits the infected cells. The cleavage results in two subunits, S1 and S2. S1
93 contains a receptor binding domain, and S2 the membrane fusion effector. An additional
94 proteolytic cleavage in the S2 subunit occurs at the site S2' during virus entry to trigger the fusion
95 of the viral envelope with the host cell membrane. The transmembrane serine protease 2
96 (TMPRSS2), a cell surface trypsin-like protease (20), and cathepsin L, an endolysosomal cysteine
97 protease (21), have both been proposed to be involved in the cleavage at the S2' site (5, 7, 17,
98 22, 23). Still, the timing and dynamics of proteolytic cleavages and their potential role in SARS-
99 CoV-2 activation, fusion, and entry remain unclear.

100 SARS-CoV-2 primarily targets cells of the lung epithelium but is also found in many other
101 epithelial tissues as it spreads throughout the host. The fact that epithelia express ACE2,

102 TMPRSS2, and cathepsin L most likely differentially influences the cell entry mechanisms of
103 SARS-CoV-2 in a specific manner. In the present study, we developed sensitive, quantitative
104 assays to analyze the SARS-CoV-2 entry process in different epithelial cell types. Using these
105 assays, we determined SARS-CoV-2 dependence on low pH, proteolytic processing, proteases-
106 and endosomal acidification-requiring dynamics, endocytosis, and protease-activated membrane
107 fusion. Our work established that SARS-CoV-2 shares with MERS-CoV and other CoVs the ability
108 to make a differential use of host cell proteases to enter and infect target cells.

109 **Results**

110 **Characterization of SARS-CoV-2 Life Cycle in Caco-2 and Vero Cells**

111 Many epithelial cell types have been reported to support productive SARS-CoV-2 infection (7),
112 and both the TMPRSS2 and cathepsin L proteases have been implicated in the proteolytic
113 processing of the viral S protein (5, 7, 17, 22, 23). We selected four epithelial cell lines that are
114 known to support SARS-CoV-2 infection, i.e., Calu-3, Caco-2, A549, and Vero cells (7). A549 are
115 intrinsically poorly infectable by SARS-CoV-2 due to the absence of the SARS-CoV-2 receptor
116 ACE2 (7). As such, we used A549 cells stably overexpressing ACE2 (A549*). When cell lysates
117 were subjected to SDS-PAGE and western blotting, we found that TMPRSS2 was effectively
118 expressed in Calu-3 cells and to a lower extent in Caco-2 cells (Fig. 1A), corroborating results
119 from others (24). Regardless of the presence of TMPRSS2, cathepsin L (from 25 to 31 kDa) and
120 its inactive form, i.e., procathepsin L (35 to 41 kDa), were present in all the cell lines (Fig. 1B).
121 However, the conversion of procathepsin L to cathepsin L appeared significantly higher in Vero
122 cells than in the three other cell lines.

123 To address how the presence or absence of TMPRSS2 influences the SARS-CoV-2
124 infectious penetration, and how the endosomal acidification contributes to the process, we aimed
125 to compare cell lines expressing or not this protease. To this end, we first defined the timing for a
126 single round of infection using our cell lines. Calu-3 and Caco-2 served as TMPRSS2-positive
127 (TMPRSS2+) cells, and A549* and Vero as non-expressing cells. The susceptibility of Caco-2 and
128 Vero cells to SARS-CoV-2 at multiplicities of infection (MOIs) of 0.1 and 0.5, respectively, was
129 assessed by fluorescence microscopy after immunostaining with a mouse monoclonal antibody
130 (mAb) against the intracellular viral nucleoprotein NP (Fig. 1C). Results show that 10% of Caco-2
131 cells were positive for NP at 8 hours post-infection (hpi). Similarly, 35% of Vero cells were found
132 infected at 8 hpi (Fig. 1C).

133 To quantify infection more accurately, we then performed flow cytometry analysis of Caco-
134 2 and Vero cells infected with different MOIs of SARS-CoV-2 (Fig. 1D and E). The fluorescence

135 increased over time and reached a plateau within 16 to 24 hpi (Fig. 1E), showing that the signal
136 detected in the flow cytometry-based assays corresponded to viral replication and not to input
137 particles. These kinetics were in agreement with real-time quantitative reverse transcription PCR
138 (qRT-PCR) monitoring over time the amount of SARS-CoV-2 genome (Fig. 1F).

139 To evaluate the production and release of *de novo* infectious viral particles, we infected
140 Caco-2 and Vero cells and quantified virus production up to 24 hpi by 50% tissue culture infective
141 dose assay (TCID50). Infectious progeny viruses were found to be released from infected cells as
142 early as 8-12 hpi (Fig. 1G). Virus replication kinetics and *de novo* virus release was found to be
143 similar in Calu-3 and A549* cells (data not shown). Altogether, our analysis revealed that SARS-
144 CoV-2 completes one round of infection, from virus binding and entry to replication and release of
145 *de novo* infectious particles, within 8 h in Caco-2 cells and somewhat longer in Vero cells, i.e.,
146 between 8 and 12 h. In all the further experiments, as we aimed at characterizing SARS-CoV-2
147 entry mechanisms therefore we used MOIs allowing the infection of about 20% of the cells and
148 limited our assays to 8 hpi.

149 **SARS-CoV-2 Makes a Differential Use of Host Cell Proteases for Infectious Penetration**

150 To evaluate the role of the cell surface TMPRSS2 and endolysosomal cathepsin L proteases in
151 the entry mechanisms of SARS-CoV-2, we used aprotinin and SB412515, respectively, to
152 selectively inhibit the two proteases. As expected, no noticeable effect was observed when
153 aprotinin was added to TMPRSS2-negative (TMPRSS2-) cells (A549* and Vero cells) prior to
154 infection (Fig. 2A). In agreement with previous work (25), we observed that aprotinin reduced
155 SARS-CoV-2 infection in a dose-dependent manner in the cells that express TMPRSS2 (Calu-3
156 and Caco-2 cells) (Fig. 2A). Conversely, SB412515 effectively prevented the infection of cells
157 lacking TMPRSS2 (Vero and A549* cells) in a dose-dependent manner but had no effect on
158 SARS-CoV-2 infection of Calu-3 and Caco-2 cells (Fig. 2B). The fact that aprotinin interfered with

159 SARS-CoV-2 infection in Calu-3 and Caco-2 cells indicated that, even if TMPRSS2 was blocked,
160 cathepsin L would not take over and subsequently process SARS-CoV-2.

161 We next determined the kinetics of the cathepsin L- and TMPRSS2-dependent SARS-CoV-
162 2 entry process. Cells were incubated with viruses at a low MOI (~0.9) on ice and rapidly shifted
163 to 37°C to allow virus entry and protease activity. The cathepsin L and TMPRSS2 inhibitors were
164 added at different times after warming to prevent further activation and penetration of the virus. In
165 other words, we determined the time when inhibition of SARS-CoV-2 activation is no longer
166 possible, which resulted in an increase of infection. In both TMPRSS2- cell lines (A549* and Vero
167 cells), the SB412515 add-in time course revealed that the activation by cathepsin L and the
168 subsequent infectious penetration of SARS-CoV-2 started after a 15 min lag and reached a half
169 maximal level ($t_{1/2}$) within 40-60 min (Fig. 2C). Evidently, exposure of individual viruses to
170 cathepsin L occurred non-synchronously during a time span 15-90 min after warming. The add-in
171 time course using aprotinin showed that productive penetration was much faster in TMPRSS2+
172 cells (Calu-3 and Caco-2 cells) (Fig. 2D). The $t_{1/2}$ of activation by TMPRSS2 was reached within
173 5-10 min in both cell lines. Taken together, our observations demonstrated that TMPRSS2 allowed
174 for a faster activation and penetration of SARS-CoV-2 in comparison to cells for which infection
175 depends on cathepsin L.

176 **TMPRSS2 Governs SARS-CoV-2 Dependence on Low pH for Infectious Entry**

177 Recent reports indicated that SARS-CoV-2 infection is sensitive to lysosomotropic weak bases
178 that neutralize vacuolar pH such as ammonium chloride (NH₄Cl) and chloroquine (7, 10, 11).
179 However, TMPRSS2 is active at the cell surface under neutral pH conditions (20), unlike cathepsin
180 L, which requires the low-pH environment typical of endolysosomes (21). To assess the
181 importance of endosomal acidification for infectious entry in cells expressing (Caco-2 and Calu-3)
182 and lacking (A549* and Vero) TMPRSS2, cells were exposed to SARS-CoV-2 in the presence of
183 increasing amounts of NH₄Cl or chloroquine. Our results showed that both weak bases induced a

184 dose-dependent inhibition of infection regardless of the cell type and of TMPRSS2 expression
185 (Fig. 3A and 3B). However, the dose to inhibit 50% of SARS-CoV-2 infection (IC_{50}) was found to
186 be significantly lower in cells devoid of TMPRSS2 compared to cells expressing the protease,
187 reaching a 200-fold difference for chloroquine (Table 1).

188 To validate the observation that TMPRSS2+ cells were less dependent on endosomal
189 acidification for SARS-CoV-2 infection, we made use of Bafilomycin A1 and Concanamycin B,
190 which are inhibitors of the vacuolar-type proton-ATPases (vATPases). Incubation of cells with
191 increasing amounts of the two drugs resulted in a dose-dependent inhibition of SARS-CoV-2
192 infection (Fig. 3C and 3D). Importantly, the inhibition was marginal with 10 nM of Bafilomycin A1
193 and Concanamycin B in TMPRSS2+ cells (Caco-2 and Calu-3), and the decrease in infection did
194 not exceed 50-80% at 50 nM of Concanamycin B. For comparison, infection with Uukuniemi virus
195 (UUKV), a late-penetrating virus that relies on low pH in late endosomes (LE) for penetration (26),
196 is strongly inhibited in the presence of 2 to 10 nM of Concanamycin B or Bafilomycin A1 (26).
197 From these results, it was evident that, similar to the lysosomotropic weak bases, SARS-CoV-2
198 infection appeared to be significantly less sensitive to vATPase inhibitors in TMPRSS2+ cells
199 (Caco-2 and Calu-3) in comparison to cells lacking the protease (Vero and A549* cells) (Table 1).

200 **SARS-CoV-2 Can Use Two Distinct Routes to Enter and Infect Target Cells**

201 Our results suggested that SARS-CoV-2 infection relied more on endosomal acidification in cells
202 devoid of TMPRSS2 than cells expressing the protease. To pursue this possibility, we determined
203 the kinetics of the acidification step required for the infectious penetration of SARS-CoV-2 into
204 TMPRSS2- cells. We took advantage of the fact that the neutralization of endosomal pH is nearly
205 instantaneous upon NH_4Cl addition to the extracellular medium (27). Virus particles were first
206 allowed to attach to A549* and Vero cells on ice. Entry was then synchronized by switching cells
207 rapidly to 37°C, and NH_4Cl was added at different times. In A549* and Vero cells, viruses passed
208 the NH_4Cl -sensitive step 15 min after cell warming, and the $t_{1/2}$ was reached within 50 min (Fig.

209 3E). Overall, the kinetics of SARS-CoV-2 acid-activated penetration closely resembled the time
210 course of cathepsin L-dependent activation in the absence of TMPRSS2 (Fig. 2C).

211 In Calu-3 and Caco-2 cells, both of which express TMPRSS2, it was not possible to
212 determine the timing of the acid-requiring step. We failed to detect SARS-CoV-2-infected cells
213 even by adding NH₄Cl several hours after transferring the cells from 4 to 37°C (Fig. 3E). In samples
214 where NH₄Cl was omitted, infection was readily detectable with 17% of Calu-3 and Caco-2 cells
215 infected (data not shown) suggesting that the weak base interferes with SARS-CoV-2 replication
216 in these two cell lines. It is highly likely that NH₄Cl disrupts TMPRSS2+ cell-specific functions that
217 are important for SARS-CoV-2 replication. NH₄Cl not only neutralizes the intracellular pH but also
218 alters all endosomal, lysosomal, and trans-Golgi-network functions that are acid dependent (28).

219 As an alternative method to alter endosomal pH, we used Concanamycin B instead of NH₄Cl
220 and added the vATPase inhibitor to Caco-2-cell-bound virus at different times after warming. The
221 time course showed that SARS-CoV-2 infection was insensitive to the Concanamycin B add-in as
222 early as a few seconds after shifting Caco-2 cells to 37°C (Fig. 3F). In a marked contrast, infectious
223 entry of UUKV started after 15 min and had not reached a maximum 2 h after cell warming. As
224 expected, SARS-CoV-2 passed the Concanamycin B-sensitive step in Vero cells within less than
225 15 min, and infectious entry reached a plateau value after 45 min, somewhat faster than in using
226 NH₄Cl (Fig. 3E). This difference in Vero sensitivity to endosomal pH may be that Concanamycin
227 B not only interferes with endosomal functions that are acid dependent but also indirectly with the
228 maturation of endosomes. However, unlike NH₄Cl, it was apparent that Concanamycin B had no
229 adverse effect on SARS-CoV-2 replication in all these experiments. Taken together, these results
230 strongly suggested that SARS-CoV-2 can use two different routes to enter and infect target cells,
231 i.e., fast pH-independent penetration in TMPRSS2+ cells (Fig. 2D and 3F) and slow acid-activated
232 entry in cells lacking TMPRSS2 (Fig. 2C and 3E).

233 **SARS-CoV-2 Relies on Endolysosomal Maturation for Infection of TMPRSS2- Cells**

234 The timing of acid-dependent and protease-activated steps suggested that SARS-CoV-2
235 penetration might occur from endolysosomes in cells devoid of TMPRSS2 and from the plasma
236 membrane or early endosomes (EEs) in TMPRSS2+ cells. To determine whether SARS-CoV-2
237 requires reaching the endolysosomal compartments for the productive infection of TMPRSS2-
238 cells, we exploited the small GTPase Rab7a, which is a key player of LE maturation and function.

239 TMPRSS2- Vero cells were transfected with DNA plasmids encoding the wild-type (wt), the
240 dominant-negative (Rab7a T22N), and the constitutively active (Rab7a Q67L) forms of Rab7a
241 tagged with the enhanced green fluorescent protein (EGFP) prior to infection with SARS-CoV-2.
242 Transfected cells were selected for different levels of EGFP expression and then analyzed for
243 infection. Increasing expression of the wt molecule of Rab7a facilitated SARS-CoV-2 infection. On
244 the contrary, increasing expression of both mutants of Rab7a, which abrogates the maturation of
245 newly formed LEs (26, 29), resulted in a 50% decrease in infection (Fig. 4A), indicating that the
246 virus cannot fuse in Rab7a T22N- and Q67L-late endosomal vesicles. This result suggested that
247 proper maturation of LEs is mandatory for the cathepsin L-dependent infectious entry of SARS-
248 CoV-2.

249 LE maturation relies on microtubule-mediated transport to the nuclear periphery and
250 proteasome activity (26, 29). Treatment of Vero cells with colcemid, a drug that interferes with
251 microtubule polymerization, resulted in a 30%-45% decrease in infection (Fig. 4B). Additionally,
252 late endosomal penetration of IAV and UUKV has been shown to be sensitive to free ubiquitin
253 depletion produced by the proteasome inhibitor MG-132 (26, 30). Therefore, to determine if free
254 ubiquitin was required for SARS-CoV-2 infection, A549* and Vero cells were treated with MG-132.
255 Results show that SARS-CoV-2 infection was strongly inhibited in the presence of MG-132 in both
256 cell lines (Fig. 4C). The calculated IC₅₀ confirmed the high proficiency (4 to 17 nM) of MG-132 to
257 interfere with the cathepsin L-mediated SARS-CoV-2 entry route (Table 1).

258 To determine the kinetic of the MG-132-sensitive step in the entry process, we followed the
259 same experimental procedure used to determine the kinetics of endosomal acidification-
260 dependent and cathepsin L-mediated activation of SARS-CoV-2 (Fig. 2C and 3E) but utilizing MG-
261 132 instead of protease inhibitor and NH₄Cl. Briefly, viruses were bound to A549* and Vero cells
262 at a low MOI on ice, and then promptly switched to 37°C before adding MG-132 at different times.
263 After a 15 min lag, infectious penetration occurred asynchronously between 30 and 60 min, with
264 a $t_{1/2}$ within 40-50 min (Fig. 4D). This time course was consistent with endolysosomal maturation,
265 which usually lasts 30-60 min (31). Altogether, these results show that the cathepsin L-dependent
266 SARS-CoV-2 infection depends on endolysosome maturation in TMPRSS2- A549* and Vero cells.

267 Interestingly, LE maturation was also required in TMPRSS2+ cells (Calu-3 and Caco-2 cells)
268 as SARS-CoV-2 infection was reduced by colcemid in a dose-dependent manner in both cell lines
269 (Fig. 4E). Though the inhibition was efficient, the IC₅₀ values of MG-132 were one to three logs
270 higher in TMPRSS2+ cells compared to TMPRSS2- cells (Fig. 4F). As shown in Fig. 4G, infection
271 of Calu-3 and Caco-2 cells was not readily detectable when MG-132 was added 2 hpi. Together,
272 the data suggest that MG-132 impaired viral replication in these assays and not the TMPRSS2-
273 dependent SARS-CoV-2 entry process.

274 **Low pH Is Not Essential for SARS-CoV-2 Membrane Fusion**

275 The penetration of enveloped viruses into the cytosol involves fusion between the viral envelope
276 and a cell membrane. In most cases, endosomal acidification contributes to activate viral
277 glycoproteins and is used as a cue to trigger fusion (12). SARS-CoV-2 does not rely on endosomal
278 acidification to enter TMPRSS2+ cells, which suggests that the virus does not rely on low pH for
279 membrane fusion but solely for the activation of cathepsin L in cells lacking TMPRSS2.

280 To examine the requirement of pH acidification for the SARS-CoV-2 membrane fusion
281 mechanisms, we first assessed the possibility to inactivate the virus with acidic buffers prior
282 infection. In such an assay, the virus undergoes a transition toward the post-fusion state at the

283 optimal pH. If the transition is irreversible, the spike protein is no longer able to fuse with target-
284 cell membranes, and thus, the viral particles are rendered non-infectious. With this approach, we
285 found that about 50% of viruses were still infectious in Caco-2 and Vero cells, even after an
286 exposition to buffers at pH ~5 for 10 min (Fig. 5A). Semliki forest virus (SFV) is an early-penetrating
287 virus that has a Class-II viral fusion glycoprotein with an irreversible priming step triggered at a
288 pH-activation threshold of 6.2 (26). In contrast to SARS-CoV-2, infection by low pH-pretreated
289 SFV was reduced by 70-80% at pH ~6.0 and below (Fig. 5B).

290 To further investigate the influence of low pH on SARS-CoV-2 fusion, we then evaluated the
291 capacity of SARS-CoV-2 to mediate cell-cell fusion (“fusion-from-within”) as described for
292 unrelated viruses (32). To this end, we used Vero cells as they are negative for TMPRSS2, which
293 makes it a convenient model to monitor proteolytic activation of the S protein at the cell surface
294 by exogenous proteases. Briefly, confluent monolayers of Vero cells were infected with SARS-
295 CoV-2 for 24 h, and the infected cells were then subjected to buffers of different pH values. The
296 extent of cell-cell fusion, i.e., formation of syncytia, was determined using a fusion index that
297 expresses the average number of fusion events per original mononucleated cell (33). The index
298 reaches 1 when all the nuclei in the microscope field are present in a single cell, and the value is
299 0 when all cells have one nucleus each. Formation of syncytia with two or more nuclei was
300 observed regardless of the pH of the buffer (Fig. 5C), and the fusion index did not significantly
301 differ when cells were treated with low pH or neutral buffers (Fig. 5D). Together, our observations
302 strongly suggested that low pH is not required for the SARS-CoV-2 fusion mechanisms.

303 **Proteolytic Processing Is Sufficient and Necessary for SARS-CoV-2 Fusion**

304 The results suggested that acidification is not required to prompt viral fusion and that proteolytic
305 processing might be sufficient. As furin and TMPRSS2 are believed to mediate the activation of
306 the SARS-CoV-2 spike proteins, we then evaluated the ability of the two proteases to trigger
307 SARS-CoV-2 activation and fusion using our flow cytometry-based infection analysis and syncytia-

308 forming assay. In the following series of experiments, exogenous trypsin was used to mimic
309 TMPRSS2 at the cell surface as the two enzymes are closely related and both belong to the group
310 of trypsin-like proteases. The use of exogenous cathepsin L was excluded because the enzyme
311 is only active at pH ~5, which would have made it impossible to distinguish between an effect due
312 to low pH or proteolytic cleavage.

313 Viral particles were first subjected to proteases prior to being added to Caco-2 and Vero
314 cells. We found that infection increased as much as 2- to 3-fold following the SARS-CoV-2
315 proteolytic processing by trypsin, whereas the pre-exposure of particles to furin had no apparent
316 effect (Fig. 6A). Similar results were obtained with our cell-cell fusion assay. Large syncytia with
317 five or more nuclei were observed when infected Vero cells were exposed to trypsin (Fig. 6B).
318 Contrary to trypsin-treated cells, no difference was observed after furin treatment in comparison
319 to the mock-treated samples, for which the only cells with more than one nucleus were those
320 dividing (Fig. 6B). Additionally, the fusion index in Vero cells was increased under trypsin treatment
321 compared to mock- and furin-treated cells (Fig. 6C). Altogether our data indicated that proteolytic
322 cleavage is sufficient and necessary for SARS-CoV-2 membrane fusion.

323 **Endosomal Acidification Is Required for Endolysosomal Proteases Priming Viral Fusion**

324 Our results support a model where endosomal acidification is not essential for SARS-CoV-2
325 membrane fusion, but SARS-CoV-2 infection relies on low pH for cathepsin L-dependent infection
326 in cells lacking TMPRSS2. Therefore, we tested the possibility that acid pH is required for the
327 activation of endolysosomal proteases that in turn trigger SARS-CoV-2 fusion. In such a scenario,
328 the spike S proteins that are already primed by proteases should no longer rely on low pH for
329 fusion. Indeed, we found that the fusion index was not increased when trypsin treatment was
330 followed by exposure to a decreasing pH of 7.4 to 5 (Fig. 7A and 7B), the latter value being typical
331 of the luminal pH of endolysosomes (29).

332 To further evaluate whether SARS-CoV-2 membrane fusion is low pH-independent, viral
333 particles were then exposed to buffers at pH ~5 and subsequently subjected to proteolytic
334 cleavage by trypsin. Our results revealed that SARS-CoV-2 infectivity was preserved when viral
335 particles were exposed to the low-pH buffer prior to trypsin treatment in comparison to virus
336 particles that were solely exposed to acidic pH (Fig. 7C). The infectivity also remained preserved
337 when the virus was first subjected to trypsin and then acidification. Taken together, the results
338 showed that endosomal acidification does not play a role in SARS-CoV-2 membrane fusion,
339 whether it occurs before or after the proteolytic processing of viral particles. In addition, our results
340 strongly suggested that the potential pH-induced conformational changes in the SARS-CoV-2
341 spikes were neither irreversible nor detrimental for the viral fusion.

342 To directly test whether endosomal acidification is needed for the host cell proteases that
343 prime SARS-CoV-2 fusion, and not for the fusion mechanisms themselves, we assessed whether
344 preactivated viral particles no longer depend on endosomal acidification for infectious entry. For
345 this purpose, the proteolytic processing of the virus particles was achieved with trypsin prior to the
346 infection of A549* and Vero cells. To interfere with the acid-dependent endolysosomal proteases,
347 the infection was carried out in the continuous presence of 50 nM of Bafilomycin A1. As A549*
348 and Vero cells do not express TMPRSS2, this assay allowed us to directly test the impact of
349 extracellular protease-activated viral particles. As reported above (Fig. 3C), infection with
350 untreated viral particles was severely hampered when proton pumps were blocked in the absence
351 of TMPRSS2 (Fig. 7D). In stark contrast, the protease-preactivated viral particles remained
352 infectious in the presence of Bafilomycin A1 (Fig. 7D).

353 The capacity of SARS-CoV-2 to infect A549* and Vero cells upon proteolytic activation,
354 despite the absence of functional endolysosomal proteases, was confirmed using NH₄Cl. As
355 expected, in our synchronized infection assay, untreated particles became NH₄Cl insensitive 50
356 min post entry (Fig. 7E, 7F, and 3E). However, when the viral particles were pretreated with
357 trypsin, no sensitivity to NH₄Cl was observed (Fig. 7E and 7F). These results strongly supported

358 the view that, once activated by proteolytic cleavage, the virus is no longer dependent on
359 endosomal acidification for infection. Altogether, our data show that SARS-CoV-2 resembles other
360 CoVs in that its entry depends on diverse host cell proteases. It can use two distinct routes, where
361 either TMPRSS2 mediates its pH-independent penetration from or close to the cell surface or
362 alternatively, it is transported to endolysosomes, where low pH activates cathepsin L that in turn
363 primes viral fusion and penetration.

364 **Discussion**

365 The infectious entry process of CoVs is complex (3). Several host cell proteases can prime the
366 CoV spike S proteins for viral membrane fusion, but it is not yet known whether these mechanisms
367 require selective proteases or a coordinated, spatio-temporal combination of several proteases.
368 The importance of endosomal acidification in the productive penetration of all CoVs is also a
369 matter of debate. Furin, TMPRSS2, and cathepsin L have all three been implicated in coronavirus
370 activation for entry (5, 7, 17, 22, 23), and agents elevating endosomal pH such as chloroquine
371 have been described to interfere with infection (7, 10, 11). SARS-CoV-2 and other CoVs have
372 apparently found a way to use diverse entry mechanisms to infect target cells and spread
373 throughout the host.

374 In this study, we developed reliable and accurate assays to investigate SARS-CoV-2
375 infection in lung, intestine, and kidney epithelial cells, from proteolytic activation to membrane
376 fusion. In agreement with other reports (7, 25), our results showed that SARS-CoV-2 infection was
377 sensitive to inhibitors of TMPRSS2 and cathepsin L. We further found that blocking TMPRSS2
378 abrogated infection even when the cells were expressing cathepsin L, indicating that the virus
379 does not reach endolysosomal cathepsins when TMPRSS2 is present. Others have shown that
380 infection by MERS pseudo-viruses was suppressed by trypsin-like protease inhibitors in the
381 presence of the tetraspanin CD9, while entry was unaffected but rather blocked by cathepsin
382 inhibitors in the absence of CD9 (34). These authors proposed that tetraspanins condense CoV
383 entry factors into localized positions on or close to the cell surface, allowing rapid and efficient
384 activation of viral fusion (35).

385 We observed that SARS-CoV-2 used two distinct routes to enter cells, one fast (~10 min)
386 which corresponded to the timing of TMPRSS2 activation, and the second slower (40-50 min)
387 corresponding to cathepsin L priming. Although other cellular factors are likely necessary, our
388 results support the view that TMPRSS2 is a major determinant of the SARS-CoV-2 fast entry track.

389 Similar observations have been made for the human CoV 229E (hCoV-229E), which prefers cell-
390 surface TMPRSS2 to endosomal cathepsins for cell entry (36-38).

391 It is clear from our data that, in the presence of TMPRSS2, SARS-CoV-2 did not rely on
392 endosomal acidification for infectious penetration. Concanamycin B, which specifically inhibits
393 vATPases and elevates endosomal pH, affected UUKV, an enveloped virus that penetrates host
394 cells by acid-activated membrane fusion (26), but not SARS-CoV-2. This was consistent with
395 reports that TMPRSS2 processes CoV S and other substrates at or nearby the plasma membrane
396 (39, 40), i.e., at neutral pH. Using aprotinin, we found that half of the bound viral particles required
397 5-10 min to pass the TMPRSS2-dependent step. We cannot completely exclude that aprotinin
398 was not instantaneously effective when it was added to the infected cells. In this case, the timing
399 of TMPRSS2-requiring step was therefore faster. SARS-CoV-2 activation and penetration would
400 then likely take place at the plasma membrane following proteolytic activation, as proposed for
401 hCoV-229E and MERS-CoV (37, 41).

402 An alternative scenario would be that SARS-CoV-2 is sorted into the endocytic machinery
403 regardless of the TMPRSS2 expression. The time course of TMPRSS2-requiring step resembled
404 that of cargo sorted into EEs, *circa* 5-10 min (31). Another observation supporting this hypothesis
405 was that colcemid hampered infection. This drug perturbs LE maturation by disrupting the
406 microtubule network, and in turn, causes the accumulation and dysfunction of EEs (26). Such a
407 strategy has been proposed for reoviruses, which use similar uptake but different trafficking
408 depending on whether viral particles are activated or not (42). Like other CoVs (39), more
409 functional investigations are required to determine, where exactly, from the plasma membrane or
410 EEs, SARS-CoV-2 enters the cytosol of TMPRSS2+ cells, and whether the processing of the S
411 protein is followed by transport of the virus to downstream organelles for penetration.

412 In the absence of TMPRSS2, it was evident that SARS-CoV-2 was dependent on
413 endocytosis and transport through the late endosomal system for infectious penetration. Infectious
414 entry was inhibited by endosomal-pH neutralizing drugs. Impairing LE maturation by either

415 colcemid or the expression of Rab7a T22N affected SARS-CoV-2 infection. The sensitivity to MG-
416 132 mirrored observations with UUKV, IAV, and murine CoVs, which accumulated in cytosolic
417 vesicles and failed to infect (26, 30, 43). Others have reported that SARS-CoV-2 depends on
418 PIKfyve for the infection of 293T cells, a line devoid of TMPRSS2 (10). PIKfyve is a
419 phosphoinositide kinase involved in the first stages of LE maturation. Collectively, our results
420 indicate that SARS-CoV-2, like other CoVs (41, 44, 45), has a dependence on functional
421 endolysosomes and cathepsins for infectious penetration when the viral particles are not activated
422 at or near the cell surface.

423 Our results suggested that the proteolytic activation of the spike S protein was sufficient and
424 necessary for SARS-CoV-2 fusion. The Vero cells used in our virus-mediated cell-cell fusion assay
425 did not express TMPRSS2 on the cell surface. In this assay, exogenous furin failed to promote
426 the syncytia formation, indicating that either furin was inefficient or not sufficient to achieve the full
427 activation of the SARS-CoV-2 protein S at the plasma membrane. The S1/S2 site exhibits a RRAR
428 motif instead the typical RX(R/K)R furin one, and a recent structural study support the view that
429 the cleavage by furin at this site in the S trimers is rather low, about 30% (17, 46, 47). However,
430 we found that, unlike furin, trypsin prompted the formation of syncytia, which rather supports the
431 involvement of proteases in the target cells, such as TMPRSS2 and cathepsin L, to complete the
432 proteolytic processing of the S protein. Others have shown that SARS-CoV-2, and also MERS-
433 CoV, mediate cell-cell fusion at neutral pH without any further proteolytic treatment when target
434 cells express TMPRSS2 (16, 48).

435 It is also apparent from our results that the SARS-CoV-2 progeny was not fully processed
436 and activated. Trypsin pretreatment increased the virus infectivity. More work is evidently required
437 to decipher the SARS-CoV-2 fusion mechanism. The list of the involved host cell proteases is
438 most likely not restricted to TMPRSS2 and cathepsin L, as suggested by a recent biochemistry
439 study (49). The S proteolytic activation might involve the cleavage of other sites than S1/S2 and
440 S2', similarly to what was found for the MERS-CoV protein S (40). It is, however, tempting to

441 postulate that the cleavage between S1 and S2 is not complete on SARS-CoV-2 particles, with
442 only one or two of the three S1/S2 sites cut by furin within S trimers. In this model, cutting all the
443 S1/S2 sites would be achieved by proteases in target cells such as TMPRSS2 and cathepsin L.
444 The fusogenic conformational change would then occur and be completed by the cleavage of the
445 S2' sites, therefore, unmasking the fusogenic units. The S1/S2 site significantly differs in amino-
446 acid residues through CoVs (17) and highly likely influences the overall viral fusion process.

447 We found that the level of virus mRNA and infectious viral progeny released in the outer
448 media was lower in the absence of TMPRSS2. The TMPRSS2-dependent entry mechanisms
449 occurred faster than the cathepsin L-activated pathway, and it might be that the early route results
450 in a more productive infection than the late-penetrating process. Separate studies support, at least
451 for some CoV strains including HCoV-229E, the view that early entry results in productive
452 infection, while late penetration would be an alternative, backup route (35, 37, 38). Other works
453 on therapeutics have linked host cell proteases to CoV spread. Inhibitors of TMPRSS2, but not of
454 cathepsins, effectively prevent the pathogenesis of SARS-CoV in mice, suggesting that SARS-
455 CoV mainly uses cell surface proteases rather than endosomal cathepsins *in vivo* (50). The
456 identification of all host cell proteases involved in SARS-CoV-2 and other CoV infection, as well
457 as the tissues and organs that express them, remains an important objective to better understand
458 viral propagation and induced diseases.

459 Intriguingly, SARS-CoV-2 showed a strong resistance to acidic buffers. Exposure to pH ~5.0
460 only marginally inactivated the virus, and infectivity was even rescued and enhanced by proteolytic
461 treatment. In addition, trypsin activation appeared to protect the virus from acid inactivation, which
462 could explain how it is found to infect the gastrointestinal tract *in vivo*. SARS-CoV-2 has evidently
463 developed a remarkable ability to adapt to an acidic environment. Interestingly, low pH has been
464 shown to switch the positioning of the receptor-binding domain in the SARS-CoV-2 S trimers,
465 which could help the virus to escape the immune system (51). Overall, this property certainly

466 confers the virus the ability to sustain a high infectivity, not only within endosomes to enter host
467 cells, but also in the extracellular space, especially during the virus spread throughout the host.

468 Reports on the cell entry of SARS-CoV-2 and other CoVs often describe only one cell model
469 system, and the literature in this field remains confusing in general. Our study recapitulates within
470 a single investigation the SARS-CoV-2 entry process and provides an overview of the cellular
471 mechanisms used by SARS-CoV-2 to penetrate and infect target cells. Although it remains to be
472 confirmed under physiological conditions, we propose that SARS-CoV-2 can enter cells through
473 two distinct, mutually exclusive pathways. When target cells express TMPRSS2, the virus is
474 activated at or close to the cell surface and penetrates early in a pH-independent manner. When
475 target cells are devoid of TMPRSS2, SARS-CoV-2 is endocytosed and sorted into the
476 endolysosomes from where the virus is activated in a pH-dependent manner and penetrates the
477 cytosol late. With the ability to subvert diverse cell entry routes, SARS-CoV-2 has likely found a
478 way to expand the number of target tissues and organs, which certainly contributes to the broad
479 tropism of the virus *in vivo*.

480 **Materials and Methods**

481 **Cells**

482 The African green monkey Vero kidney epithelial cells (ATCC CRL 1586), the human Caco-2
483 colorectal adenocarcinoma (ATCC HTB-37), the human Calu-3 lung adenocarcinoma (ATCC
484 HTB-55), and the human epithelial lung cells A549 stably expressing ACE2 (A549*; a kind gift
485 from Prof. Ralf Bartenschlager) were all maintained in Dulbecco's modified Eagle's medium
486 (DMEM) supplemented with 10% fetal bovine serum (FBS) and 100 units.mL⁻¹ penicillin, and 100
487 µg.mL⁻¹ streptomycin. Baby hamster kidney cells (BHK-21) were grown in Glasgow's minimal
488 essential medium containing 10% tryptose phosphate broth, 5% FBS, 100 units.mL⁻¹ penicillin,
489 and 100 µg.mL⁻¹ streptomycin. All cell lines were grown in an atmosphere of 5% CO₂ in air at
490 37°C. All products used for cell culture were obtained from Thermo Fischer Scientific and Sigma-
491 Aldrich.

492 **Viruses**

493 SARS-CoV-2 (strain BavPat1) was obtained from Prof. Christian Drosten at the Charité in Berlin,
494 Germany, and provided via the European Virology Archive. The virus was amplified in Vero cells
495 and working stocks were used after three passages. Uukuniemi (UUKV) and Semliki forest (SFV)
496 viruses were previously described and amplified in BHK-21 cells (52, 53). The MOI is given
497 according to the titer determined by plaque- or foci-forming unit assay for each cell line. When
498 indicated, the titer was obtained by TCID50.

499 **Antibodies, reagents, and plasmids**

500 The mouse mAb against the SARS-CoV nucleoprotein NP (40143-MM05) was purchased from
501 Sino biologicals and used at dilutions of 1:500 for flow cytometry analysis and 1:1,000 for titration
502 in TCID50 assays. The rabbit polyclonal antibody U2 targets all the UUKV structural proteins and
503 was used at a dilution of 1:4,000 for immunohistochemistry (54). The mouse mAb 8B11A3 against
504 the UUKV nucleoprotein N was a kind gift from Ludwig Institute for Cancer Research (Stockholm,

505 Sweden) (55). The mouse mAb against the SFV glycoprotein E2 was kindly provided by Prof.
506 Margaret Kielian (Albert Einstein College of Medicine, USA). mAb 8B11A3 and mAb against SFV
507 E2 were used at a dilution of 1:400 for flow cytometry analysis. The rabbit antibodies against
508 TMPRSS2 (ab92323) and actin (A2066) were obtained from Abcam and Sigma, respectively. The
509 mouse mAb against cathepsin L (BMS1032) and α -tubulin (T5158) were bought from Thermo
510 Fisher Scientific and Sigma, respectively. Anti-mouse secondary antibodies were conjugated to
511 Alexa Fluor (AF) 405 (Molecular Probes), AF488 (Molecular Probes), IRDye 700 (LI-COR), IRDye
512 800CW (LI-COR), and horseradish peroxidase (HRP; Vector Laboratories). Anti-rabbit secondary
513 antibodies conjugated to IRDye 800CW were purchased from LI-COR. NH₄Cl (Sigma), aprotinin
514 (Cayman Chemical), and chloroquine diphosphate (Sigma) stocks were dissolved in water.
515 Bafilomycin A1 (BioViotica), Concanamycin B (BioViotica), SB412515 (Cayman Chemical),
516 colcemid (Cayman Chemical), and MG-132 (Selleck Chemicals) were all dissolved in DMSO.
517 Furin and Trypsin were purchased from R&D and Sigma, respectively. Plasmids encoding EGFP-
518 tagged Rab7a, Rab7a T22N, and Rab7a Q67L have been described elsewhere (26).

519 **Protein analysis**

520 Cells were lysed with phosphate buffer saline (PBS) containing 0.1% Triton X-100 (Merck
521 Millipore), according to a standard procedure (54). Cell lysates were then diluted in LDS sample
522 buffer (Thermo Fisher Scientific) and analyzed by SDS-PAGE (Nu-PAGE Novex 10% Bis-Tris
523 gels; Thermo Fisher Scientific). Proteins were subsequently transferred to polyvinylidene
524 difluoride membranes (iBlot transfer stacks; Thermo Fisher Scientific). The membranes were first
525 blocked with Intercept blocking buffer (LI-COR) and then incubated with primary antibodies against
526 TMPRSS2, cathepsin L, actin, and α -tubulin, all diluted in Tris-buffered saline containing 0.1%
527 Tween and Intercept blocking buffer (1:1,000, 1:400, 1:5,000, and 1:2,000, respectively). After
528 extensive washing, the membranes were incubated with the corresponding secondary anti-
529 species conjugated to either IRDye 700 and 800CW (both at 1:10,000) or HRP (1:1,000). Proteins

530 were analyzed with a LI-COR Odyssey CLx scanner, or alternatively, detected with SuperSignal
531 West Pico PLUS chemiluminescent substrate (Thermo Fisher Scientific) and an iNTAS ECL
532 Chemostar analyzer.

533 **Virus infection**

534 Cells were exposed to viruses at the indicated MOIs in the presence of 2% FBS for 1 h at 37°C.
535 Virus input was then replaced by complete culture medium, and infected cells were incubated for
536 8 h before fixation. For virus-mediated cell-cell fusion, Vero cells were infected for 24 h. Cells that
537 transiently express EGFP-Rab7a and related mutants were infected 18 h post-transfection. For
538 pH-inactivation, citric acid, 2-(N-morpholino)-ethanesulfonic acid (MES), and 4-(2-hydroxyethyl)-
539 1-piperazineethanesulfonic acid (HEPES) were used as buffers at 100 mM as follow, pH < 5.5,
540 5.5 < pH < 6.5, and 6.5 < pH, respectively. Virus inputs were exposed to buffers at the indicated
541 pH for 10 min at 37°C and then to buffers at neutral pH prior infection. For furin- or trypsin-
542 activation, SARS-CoV-2 was pretreated with furin (1 $\mu\text{g.mL}^{-1}$) or trypsin (100 $\mu\text{g.mL}^{-1}$),
543 respectively, for 15 min at 37°C and allowed to infect cells. For inhibition assays, cells were
544 pretreated with drugs for 30 min at 37°C, apart from colcemid pretreatment that lasted 3 h on ice,
545 and then exposed to viruses in the continuous presence of the inhibitors. For inhibitor add-in time
546 courses, virus binding to cells was synchronized on ice for 90 min. Cells were then rapidly warmed
547 to 37°C, and SB412515 (10 μM), aprotinin (30 μM), NH₄Cl (at indicated concentrations),
548 Concanamycin B (50 nM), and MG-132 (at indicated concentrations) were added at indicated
549 times. Cells were subsequently incubated at 37°C and harvested 8 h after the warm shift. Infection
550 was monitored by either flow cytometry, fluorescence microscopy, or qRT-PCR. When infection
551 was analyzed by microscopy, cells were seeded on Lab-Tek or iBIDI glass bottom 8-well chamber
552 slides.

553 **DNA transfection**

554 As previously described (56), Vero cells were transfected with 750 ng of plasmids using
555 Lipofectamine 2000 (Invitrogen) in 24-well-plates according to the manufacturer's
556 recommendations and washed 5 h later.

557 **Immunofluorescence microscopy**

558 Fluorescence microscopy was extensively described in (57). Briefly, infected cells were rinsed
559 with PBS, permeabilized with 0.5% Triton X-100 (Sigma) for 15 min at room temperature (RT),
560 and stained with primary antibodies diluted in PBS for 1h at RT. Subsequently, cells were
561 extensively washed and incubated with secondary antibodies in the presence of 4',6-diamidino-2-
562 phenylindole (DAPI, Molecular Probes) for 45 min at RT. Samples were imaged with an
563 epifluorescence microscope Nikon Eclipse Ti-S (Nikon), whilst a Leica TCS SP8 confocal
564 microscope was used to image syncytia.

565 **Flow cytometry**

566 The flow cytometry-based infection assay has been described previously (53). Briefly, infected
567 cells were fixed with 4% formaldehyde for 30 min at RT and permeabilized with 0.1% saponin
568 (Serva). Cells were then exposed to primary antibody at RT for 1 h, washed, and subsequently
569 incubated with secondary anti-mouse antibodies at RT for another 1 h. Infected cells were
570 quantified with a FACSCelesta cytometer (Becton Dickinson) and FlowJo software (TreeStar).

571 **Virus RNA quantification**

572 As previously reported (58), RNA was harvested from cells using the NuceloSpin RNA extraction
573 kit (Machery-Nagel) according to manufacturer's instructions. The cDNA was synthesized using
574 iSCRIPT reverse transcriptase (BioRad) from 250 ng of total RNA as per supplier
575 recommendations. q-PCR was performed using iTaq SYBR green (BioRad) following the
576 manufacturer's instructions for the SARS-CoV-2 genome using the forward primer,

577 GCCTCTTCTCGTTCC, and the reverse primer, AGCAGCATCACCGGCC. HPRT1 was used as a
578 housekeeping gene using the forward primer, CCTGGCGTCGTGATTAGTGAT, and reverse
579 primer, AGACGTTCAGTCCTGTCCATAA.

580 **Virus titration by TCID₅₀ assay**

581 Confluent monolayers of Vero and Caco-2 cells in 96-well plates were infected with 10-fold serial
582 dilutions of SARS-CoV-2. Infected cells were fixed 24 hpi and subjected to immunostaining using
583 the primary mouse mAb anti-SARS-CoV-2 NP and then the secondary anti-mouse antibody
584 800CW (1:10,000). Samples were finally scanned on LI-COR.

585 **Cell-cell fusion**

586 Infected cells were washed in PBS and treated with DMEM containing 0.2% bovine serum albumin
587 (Gibco) buffered at pH 7.4, 6.0, or 5.0 using 30 mM of HEPES, MES, or citric acid, respectively,
588 for 5 min at 37°C. Alternatively, infected cells were exposed to furin (1 $\mu\text{g.mL}^{-1}$) and trypsin (100
589 $\mu\text{g.mL}^{-1}$) for 5 min at 37°C, and when indicated, followed by acidification of the culture medium as
590 described above. Subsequently, cells were washed and incubated in complete medium for 50 min,
591 and the cytosol stained with CellMask Deep Red (1:1,000, Molecular Probes) for 10 min at 37°C.
592 After fixation, cells were rinsed with PBS, and nuclei stained with Hoechst 33258 (0.5 $\mu\text{g.mL}^{-1}$,
593 Thermo Fisher Scientific). Syncytia were monitored by fluorescence microscopy as described
594 below. Fusion was quantified by counting the number of cells and nuclei present in a microscope
595 field. A fusion index (f) was calculated according to the equation $f = (1 - [c/n])$, where c is the
596 number of cells in a field after fusion and n the number of nuclei. An average field contained 50-
597 60 nuclei.

598 **Statistical analysis**

599 The data shown are representative of at least three independent experiments. Values are given
600 as the means of duplicate \pm standard error of mean or triplicates \pm standard deviations. Graph

601 plotting of numerical values, as well as the statistics, were achieved with GraphPad Prism v5.00
602 (GraphPad Software). Statistical methods and parameters are indicated in the figure legends
603 when applicable. P-values are shown when statistical differences are significant.

604 **Acknowledgments**

605 This work was supported by grants from CellNetworks Research Group funds, Heidelberg, and
606 from the Deutsche Forschungsgemeinschaft (DFG) project numbers LO-2338/1-1 and LO-2338/3-
607 1) to PYL, project numbers 415089553 (Heisenberg program), 240245660 (SFB1129),
608 278001972 (TRR186), and 272983813 (TRR179) to SB, and project 416072091 to MS. This work
609 was also supported by INRAE starter funds, IDEX-Impulsion 2020 (University of Lyon), and
610 FINOVI (Fondation pour l'Université de Lyon), all to PYL. We acknowledge funding from the
611 German Academic Exchange Service (DAAD, Research Grant 57440921) to PD. We thank Felix
612 Rey and Ari Helenius for fruitful discussions.

613 **References**

614 1. Modrow S, Falke D, Truyen U, & Schätzl H (2013) Viruses with Single-Stranded, Positive-
615 Sense RNA Genomes. *Molecular Virology*, eds Modrow S, Falke D, Truyen U, & Schätzl H
616 (Springer, Berlin, Heidelberg), pp 185-349.

617 2. Paules CI, Marston HD, & Fauci AS (2020) Coronavirus Infections-More Than Just the
618 Common Cold. *JAMA* 323(8):707-708.

619 3. Hartenian E, *et al.* (2020) The molecular virology of coronaviruses. *J Biol Chem*
620 295(37):12910-12934.

621 4. Caly L, *et al.* (2020) Isolation and rapid sharing of the 2019 novel coronavirus (SARS-CoV-2)
622 from the first patient diagnosed with COVID-19 in Australia. *Med J Aust* 212(10):459-462.

623 5. Matsuyama S, *et al.* (2020) Enhanced isolation of SARS-CoV-2 by TMPRSS2-expressing
624 cells. *Proceedings of the National Academy of Sciences of the United States of America*
625 117(13):7001-7003.

626 6. Turonova B, *et al.* (2020) In situ structural analysis of SARS-CoV-2 spike reveals flexibility
627 mediated by three hinges. *Science* 370(6513):203-208.

628 7. Hoffmann M, *et al.* (2020) SARS-CoV-2 Cell Entry Depends on ACE2 and TMPRSS2 and Is
629 Blocked by a Clinically Proven Protease Inhibitor. *Cell* 181(2):271-280 e278.

630 8. Clausen TM, *et al.* (2020) SARS-CoV-2 Infection Depends on Cellular Heparan Sulfate and
631 ACE2. *Cell*.

632 9. Daly JL, *et al.* (2020) Neuropilin-1 is a host factor for SARS-CoV-2 infection. *Science*.

633 10. Ou X, *et al.* (2020) Characterization of spike glycoprotein of SARS-CoV-2 on virus entry and
634 its immune cross-reactivity with SARS-CoV. *Nat Commun* 11(1):1620.

635 11. Wang M, *et al.* (2020) Remdesivir and chloroquine effectively inhibit the recently emerged
636 novel coronavirus (2019-nCoV) in vitro. *Cell Res* 30(3):269-271.

637 12. Harrison SC (2015) Viral membrane fusion. *Virology* 479-480:498-507.

638 13. Walls AC, *et al.* (2020) Structure, Function, and Antigenicity of the SARS-CoV-2 Spike
639 Glycoprotein. *Cell* 181(2):281-292 e286.

640 14. Wrapp D, *et al.* (2020) Cryo-EM structure of the 2019-nCoV spike in the prefusion
641 conformation. *Science* 367(6483):1260-1263.

642 15. Lai AL, Millet JK, Daniel S, Freed JH, & Whittaker GR (2017) The SARS-CoV Fusion Peptide
643 Forms an Extended Bipartite Fusion Platform that Perturbs Membrane Order in a Calcium-
644 Dependent Manner. *J Mol Biol* 429(24):3875-3892.

645 16. Buchrieser J, *et al.* (2020) Syncytia formation by SARS-CoV-2-infected cells. *EMBO*
646 *J*:e106267.

647 17. Bestle D, *et al.* (2020) TMPRSS2 and furin are both essential for proteolytic activation of
648 SARS-CoV-2 in human airway cells. *Life Sci Alliance* 3(9).

649 18. Coutard B, *et al.* (2020) The spike glycoprotein of the new coronavirus 2019-nCoV contains
650 a furin-like cleavage site absent in CoV of the same clade. *Antiviral Res* 176:104742.

651 19. Hoffmann M, Kleine-Weber H, & Pohlmann S (2020) A Multibasic Cleavage Site in the Spike
652 Protein of SARS-CoV-2 Is Essential for Infection of Human Lung Cells. *Mol Cell* 78(4):779-
653 784 e775.

654 20. Choi SY, Bertram S, Glowacka I, Park YW, & Pohlmann S (2009) Type II transmembrane
655 serine proteases in cancer and viral infections. *Trends Mol Med* 15(7):303-312.

656 21. Mohamed MM & Sloane BF (2006) Cysteine cathepsins: multifunctional enzymes in cancer.
657 *Nat Rev Cancer* 6(10):764-775.

658 22. Shang J, *et al.* (2020) Cell entry mechanisms of SARS-CoV-2. *Proceedings of the National*
659 *Academy of Sciences of the United States of America* 117(21):11727-11734.

660 23. Liu T, Luo S, Libby P, & Shi GP (2020) Cathepsin L-selective inhibitors: A potentially promising
661 treatment for COVID-19 patients. *Pharmacol Ther* 213:107587.

662 24. Zecha J, *et al.* (2020) Data, Reagents, Assays and Merits of Proteomics for SARS-CoV-2
663 Research and Testing. *Mol Cell Proteomics* 19(9):1503-1522.

664 25. Bojkova D, *et al.* (2020) Aprotinin Inhibits SARS-CoV-2 Replication. *Cells* 9(11).

665 26. Lozach PY, *et al.* (2010) Entry of bunyaviruses into mammalian cells. *Cell host & microbe*
666 7(6):488-499.

667 27. Ohkuma S & Poole B (1978) Fluorescence probe measurement of the intralysosomal pH in
668 living cells and the perturbation of pH by various agents. *Proceedings of the National
669 Academy of Sciences of the United States of America* 75(7):3327-3331.

670 28. Helenius A (2013) Virus entry: what has pH got to do with it? *Nat Cell Biol* 15(2):125.

671 29. Lozach PY, Huotari J, & Helenius A (2011) Late-penetrating viruses. *Current opinion in
672 virology* 1(1):35-43.

673 30. Khor R, McElroy LJ, & Whittaker GR (2003) The ubiquitin-vacuolar protein sorting system is
674 selectively required during entry of influenza virus into host cells. *Traffic* 4(12):857-868.

675 31. Huotari J & Helenius A (2011) Endosome maturation. *EMBO J* 30(17):3481-3500.

676 32. Bratt MA & Gallaher WR (1969) Preliminary analysis of the requirements for fusion from within
677 and fusion from without by Newcastle disease virus. *Proceedings of the National Academy of
678 Sciences of the United States of America* 64(2):536-543.

679 33. White J, Matlin K, & Helenius A (1981) Cell fusion by Semliki Forest, influenza, and vesicular
680 stomatitis viruses. *The Journal of cell biology* 89(3):674-679.

681 34. Earnest JT, *et al.* (2017) The tetraspanin CD9 facilitates MERS-coronavirus entry by
682 scaffolding host cell receptors and proteases. *PLoS pathogens* 13(7):e1006546.

683 35. Hantak MP, Qing E, Earnest JT, & Gallagher T (2019) Tetraspanins: Architects of Viral Entry
684 and Exit Platforms. *J Virol* 93(6).

685 36. Bertram S, *et al.* (2013) TMPRSS2 activates the human coronavirus 229E for cathepsin-
686 independent host cell entry and is expressed in viral target cells in the respiratory epithelium.
687 *J Virol* 87(11):6150-6160.

688 37. Shirato K, Kanou K, Kawase M, & Matsuyama S (2017) Clinical Isolates of Human
689 Coronavirus 229E Bypass the Endosome for Cell Entry. *J Virol* 91(1).

690 38. Shirato K, Kawase M, & Matsuyama S (2018) Wild-type human coronaviruses prefer cell-
691 surface TMPRSS2 to endosomal cathepsins for cell entry. *Virology* 517:9-15.

692 39. Wang L & Xiang Y (2020) Spike Glycoprotein-Mediated Entry of SARS Coronaviruses.
693 *Viruses* 12(11).

694 40. Kleine-Weber H, Elzayat MT, Hoffmann M, & Pohlmann S (2018) Functional analysis of
695 potential cleavage sites in the MERS-coronavirus spike protein. *Sci Rep* 8(1):16597.

696 41. Qian Z, Dominguez SR, & Holmes KV (2013) Role of the spike glycoprotein of human Middle
697 East respiratory syndrome coronavirus (MERS-CoV) in virus entry and syncytia formation.
698 *PLoS One* 8(10):e76469.

699 42. Boulant S, *et al.* (2013) Similar uptake but different trafficking and escape routes of reovirus
700 virions and infectious subvirion particles imaged in polarized Madin-Darby canine kidney cells.
701 *Mol Biol Cell* 24(8):1196-1207.

702 43. Yu GY & Lai MM (2005) The ubiquitin-proteasome system facilitates the transfer of murine
703 coronavirus from endosome to cytoplasm during virus entry. *J Virol* 79(1):644-648.

704 44. Simmons G, *et al.* (2005) Inhibitors of cathepsin L prevent severe acute respiratory syndrome
705 coronavirus entry. *Proceedings of the National Academy of Sciences of the United States of
706 America* 102(33):11876-11881.

707 45. Kawase M, Shirato K, Matsuyama S, & Taguchi F (2009) Protease-mediated entry via the
708 endosome of human coronavirus 229E. *J Virol* 83(2):712-721.

709 46. Wrobel AG, *et al.* (2020) SARS-CoV-2 and bat RaTG13 spike glycoprotein structures inform
710 on virus evolution and furin-cleavage effects. *Nat Struct Mol Biol* 27(8):763-767.

711 47. Cai Y, *et al.* (2020) Distinct conformational states of SARS-CoV-2 spike protein. *Science*
712 369(6511):1586-1592.

713 48. Shirato K, Kawase M, & Matsuyama S (2013) Middle East respiratory syndrome coronavirus
714 infection mediated by the transmembrane serine protease TMPRSS2. *J Virol* 87(23):12552-
715 12561.

716 49. Jaimes JA, Andre NM, Millet JK, & Whittaker GR (2020) Structural modeling of 2019-novel
717 coronavirus (nCoV) spike protein reveals a proteolytically-sensitive activation loop as a
718 distinguishing feature compared to SARS-CoV and related SARS-like coronaviruses. *bioRxiv*.

719 50. Zhou Y, *et al.* (2015) Protease inhibitors targeting coronavirus and filovirus entry. *Antiviral*
720 *Res* 116:76-84.

721 51. Zhou T, *et al.* (2020) Cryo-EM Structures of SARS-CoV-2 Spike without and with ACE2
722 Reveal a pH-Dependent Switch to Mediate Endosomal Positioning of Receptor-Binding
723 Domains. *Cell host & microbe* 28(6):867-879 e865.

724 52. Helenius A, Kartenbeck J, Simons K, & Fries E (1980) On the entry of Semliki forest virus into
725 BHK-21 cells. *The Journal of cell biology* 84(2):404-420.

726 53. Mazelier M, *et al.* (2016) Uukuniemi Virus as a Tick-Borne Virus Model. *J Virol* 90(15):6784-
727 6798.

728 54. Lozach PY, *et al.* (2011) DC-SIGN as a receptor for phleboviruses. *Cell host & microbe*
729 10(1):75-88.

730 55. Persson R & Pettersson RF (1991) Formation and intracellular transport of a heterodimeric
731 viral spike protein complex. *The Journal of cell biology* 112(2):257-266.

732 56. Meier R, *et al.* (2014) Genome-wide small interfering RNA screens reveal VAMP3 as a novel
733 host factor required for Uukuniemi virus late penetration. *J Virol* 88(15):8565-8578.

734 57. Leger P, *et al.* (2020) NSs amyloid formation is associated with the virulence of Rift Valley
735 fever virus in mice. *Nat Commun* 11(1):3281.

736 58. Woelfl F, *et al.* (2020) Novel Toscana Virus Reverse Genetics System Establishes NSs as an
737 Antagonist of Type I Interferon Responses. *Viruses* 12(4).

738 **Figures**

739 **Fig. 1. Quantification of SARS-CoV-2 infection.** (A and B) Cells were lysed and analyzed by
740 SDS-PAGE and western blotting under non-reducing conditions (A) and reducing conditions (B).
741 A549*, ACE2-expressing A549 cells. (C) Vero and Caco-2 cells were infected with SARS-CoV-2
742 at a MOI of 0.5 and 0.1, respectively, for 8 h. Infected cells were then permeabilized and
743 immunostained against the intracellular SARS-CoV-2 nucleoprotein (NP, red). Nuclei were stained
744 with DAPI (blue) before imaging by fluorescence wide-field microscopy. (D) Vero and Caco-2 cells
745 were exposed to SARS-CoV-2 at a MOI of 0.003 and 0.3, respectively, and harvested 16 h later.
746 After fixation and permeabilization, infected cells were stained with the primary mAb against NP.
747 Infection was analyzed by flow cytometry. SSC-A, side scatter, area. (E) Infection of Vero and
748 Caco-2 cells was monitored over 24 h using the flow cytometry-based assay used for the
749 experiment shown in panel D. Infection is given as the total fluorescence associated with the NP
750 protein-positive cells. MFI, mean of fluorescence intensity. (F) SARS-CoV-2 mRNA levels were
751 quantified by qRT-PCR in both Vero and Caco-2 cells infected at MOIs of 0.5 and 0.1, respectively,
752 for up to 24 h. (G) Supernatants from infected cells were collected during the time course in F and
753 assessed for the production of new infectious viral particles using a TCID50 assay on naïve Vero
754 cells.

755 **Fig. 2. SARS-CoV-2 makes a differential use of host cell proteases for infectious**
756 **penetration.** (A and B) Cells were pre-treated at indicated concentrations of aprotinin (A) and
757 SB412515 (B), which are inhibitors of TMPRSS2 and cathepsin L, respectively. Infection with
758 SARS-CoV-2 (MOI of 0.9) was achieved in the continuous presence of drug. Infected cells were
759 quantified by flow cytometry as described in Fig. 1D, and data normalized to samples where
760 inhibitors had been omitted. (C and D) SARS-CoV-2 particles (MOI of 0.9) were bound to A549*
761 and Vero cells (C) or Calu-3 and Caco-2 cells (D) on ice for 90 min, and subsequently, warmed
762 rapidly to 37°C to allow infectious penetration. 10 µM of SB412515 (C) or 30 µM of aprotinin (D)

763 were added at different times post warming to block further proteolytic activation. Infection was
764 analyzed by flow cytometry, and data were normalized to samples where protease inhibitors had
765 been omitted.

766 **Fig. 3. SARS-CoV-2 infection depends on endosomal acidification.** (A to D) Cells were pre-
767 treated with endosomal-pH interfering drugs at indicated concentrations and subsequently
768 infected with SARS-CoV-2 in the continuous presence of drug, namely NH₄Cl (A), chloroquine (B),
769 Bafilomycin A1 (C), Concanamycin B (D). Infected cells were quantified by flow cytometry as
770 described in Fig. 1D, and data normalized to samples where inhibitors had been omitted. (E)
771 Binding of SARS-CoV-2 to cells was synchronized on ice for 90 min. Subsequently, cells were
772 rapidly shifted to 37°C to allow penetration. NH₄Cl (50 mM for A549* and Vero cells, and 75 mM
773 for Calu-3 and Caco-2 cells) was added at indicated times to neutralize endosomal pH and block
774 the acid-dependent step of SARS-CoV-2 infectious penetration. Infected cells were analyzed by
775 flow cytometry, and data normalized to samples where NH₄Cl had been omitted. (F) Same than
776 in (E) but using Concanamycin B (50 nM) instead NH₄Cl. Uukuniemi virus (UUKV) was used to
777 control the efficiency of Concanamycin B to neutralize endosomal pH in Caco-2 cells.

778 **Fig. 4. SARS-CoV-2 relies on late endosomal maturation for infection.** (A) EGFP-Rab7a wild-
779 type (wt), Q79L (constitutively active mutant), and T22N (dominant-negative mutant) were
780 transiently expressed in Vero cells. The cells were then infected with SARS-CoV-2 at a MOI
781 ~0.003. Using flow cytometry, cell populations were selected for levels of EGFP-Rab7a expression
782 in roughly one-log increments, and infected cells were quantified within each population 8 hpi.
783 Data were normalized to infection in cell populations with the lowest EGFP-Rab7a intensity.
784 Unpaired t-test with Welch's correction was applied. *, p < 0.05; **, p < 0.01. RU, relative unit. (B)
785 and C) Cells were pre-treated with colcemid (B) and MG-132 (C) at indicated concentrations and
786 subsequently infected with SARS-CoV-2 in the continuous presence of inhibitors. Infection was
787 analyzed by flow cytometry, and data were normalized to samples where inhibitors had been

788 omitted. Unpaired t-test with Welch's correction was applied. *, p < 0.05; **, p < 0.01; ****, p <
789 0.0001. (D) SARS-CoV-2 particles (MOI of 0.9) were bound to A549* and Vero cells on ice for 90
790 min, and then, switched rapidly to 37°C to allow infectious penetration. MG-132 (3.7 μ M) was
791 added to cells at indicated times to block further late endosomal maturation. Infection was
792 analyzed by flow cytometry, and data were normalized to samples where MG-132 had been
793 omitted. (E) As in the panel B but using Caco-2 cells instead Vero cells. (F) Same as C, except
794 for Calu-3 and Caco-2 cells. (G) The timing of the MG-132-sensitive step during SARS-CoV-2
795 infectious entry into Calu-3 and Caco-2 cells was assayed as detailed in D but using 60 μ M of
796 MG-132.

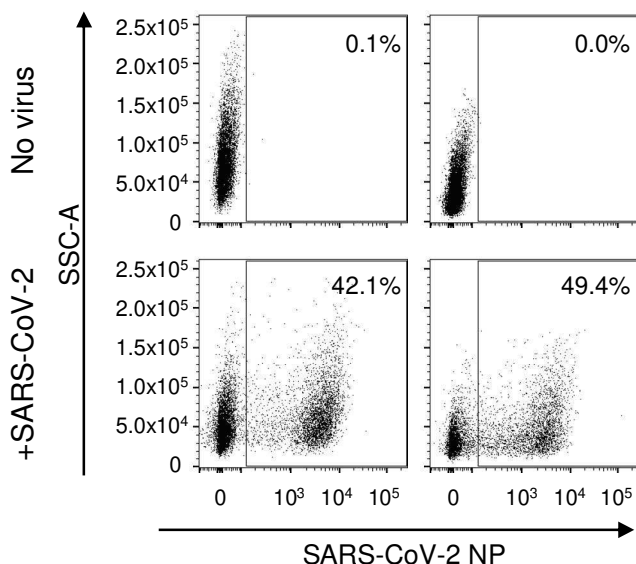
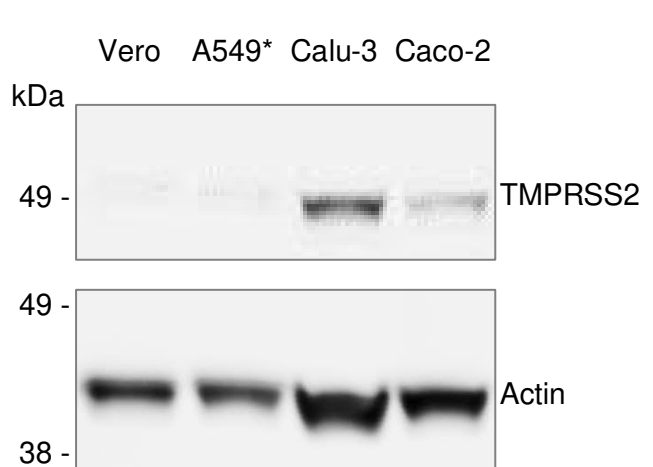
797 **Fig. 5. Acidification is not sufficient to trigger SARS-CoV-2 membrane fusion.** (A) SARS-
798 CoV-2 and (B) Semliki forest virus (SFV) particles were pre-treated at indicated pH for 10 min at
799 37°C. Viruses were subsequently neutralized with buffers at pH ~7.4 and allowed to infect Caco-
800 2 and Vero cells. Infected cells were then immunostained against the NP protein and analyzed by
801 flow cytometry. Data are normalized to samples pretreated with buffers at pH ~7.4. (C) Confluent
802 monolayers of Vero cells were infected with SARS-CoV-2 at a MOI ~0.003 for 24 h prior to
803 treatment with buffers at indicated pH for 5 min at 37°C. Plasma membrane was stained 1 h post-
804 treatment with CellMask Deep Red (red). After fixation, nuclei were stained with Hoechst (blue).
805 White stars indicate syncytia. (D) Images of microscope fields (32 < n < 44) obtained in (C) were
806 quantified. Fusion index is given as $f = 1 - [(\text{number of cells in a field after fusion}) / (\text{number of})$
807 $\text{nuclei})]$. Unpaired t-test with Welch's correction was applied. ns, non-significant.

808 **Fig. 6. Proteolytic processing triggers SARS-CoV-2 membrane fusion.** (A) SARS-CoV-2 (MOI
809 of 1.2) was subjected to pretreatment with trypsin and furin for 15 min at 37°C prior infection of
810 Caco-2 and Vero cells. Infected cells were quantified by flow cytometry as described in Fig. 1D.
811 Data were normalized to samples not pre-treated with trypsin. (B) Confluent monolayers of Vero
812 cells were infected with SARS-CoV-2 at a MOI ~0.003 for 24 h prior trypsin and furin treatment for

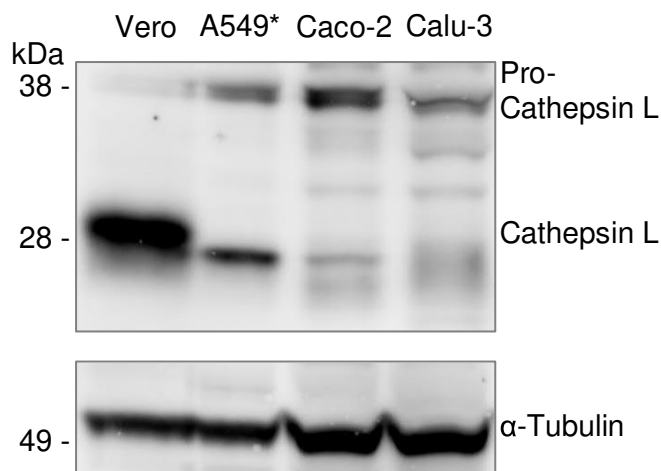
813 5 min at 37°C. Plasma membrane was stained with CellMask Deep Red (red) 1 h after
814 trypsinization. After fixation, nuclei were stained with Hoechst (blue), and cells imaged by wide-
815 field fluorescence microscopy. White stars indicate syncytia. (C) Images of microscope fields (n =
816 39, no protease, n = 63, +trypsin, and n = 54, +furin) obtained in (B) were quantified. Fusion index
817 is calculated as in Fig. 5D. Unpaired t-tests with Welch's correction was applied. **, p < 0.01.

818 **Fig. 7. SARS-CoV-2 no longer requires endosomal acidification after proteolytic**
819 **processing.** (A) Confluent monolayers of Vero cells were infected with SARS-CoV-2 at a MOI
820 ~0.003 for 24 h and then subjected to trypsin treatment for 5 min at 37°C. The cells were allowed
821 to recover for 1 h at 37°C, and subsequently, exposed to buffers at indicated pH for 5 min at 37°C.
822 Cell-cell fusion was determined as described in Fig. 6B and 6C. n > 28 microscope fields were
823 analyzed, and unpaired t-test with Welch's correction was applied. ns, non-significant. (B) Shows
824 the increase in cell-cell fusion after trypsin treatment according to pH. The fusion is given as the
825 ratio between the values obtained for trypsin-treated samples and those obtained for untreated
826 samples. (C) SARS-CoV-2 particles (MOI of 1.2) were first subjected to trypsin treatment for 15
827 min at 37°C followed by exposition to buffers at indicated pH for 10 min at 37°C, and *vice versa*.
828 A549* and Vero cells were then infected and analyzed by flow cytometry as described in Fig. 1D.
829 (D) Trypsin-activated SARS-CoV-2 (MOI ~0.003) was allowed to infect A549* and Vero cells in
830 the continuous presence of Bafilomycin A1. Infection was quantified by flow cytometry, and data
831 normalized to samples where the inhibitor had been omitted. (E and F) Binding of trypsin-activated
832 SARS-CoV-2 (MOI ~0.003) to Vero (E) and A549* (F) was synchronized on ice for 90 min.
833 Subsequently, cells were rapidly shifted to 37°C to allow penetration. NH₄Cl (50 mM) was added
834 at indicated time to neutralize endosomal pH and block the acid-dependent step of SARS-CoV-2
835 infectious penetration. Infected cells were analyzed by flow cytometry, and data normalized to
836 samples where NH₄Cl had been omitted.

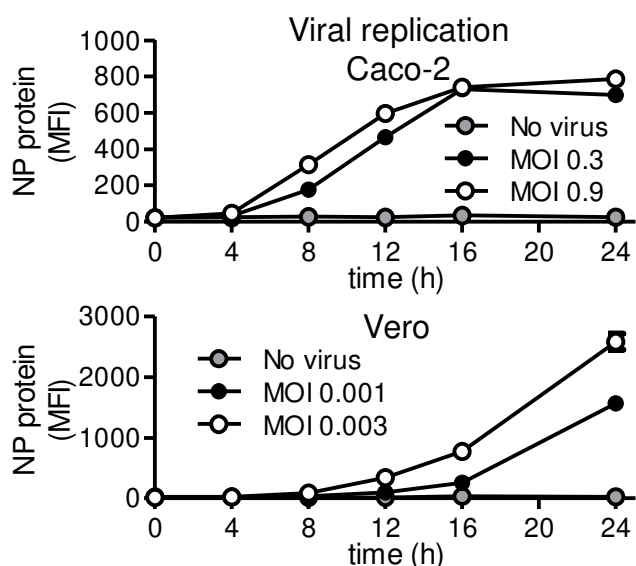
837 **Table 1. Half maximal inhibitory (IC₅₀) of inhibitors against SARS-CoV-2.**



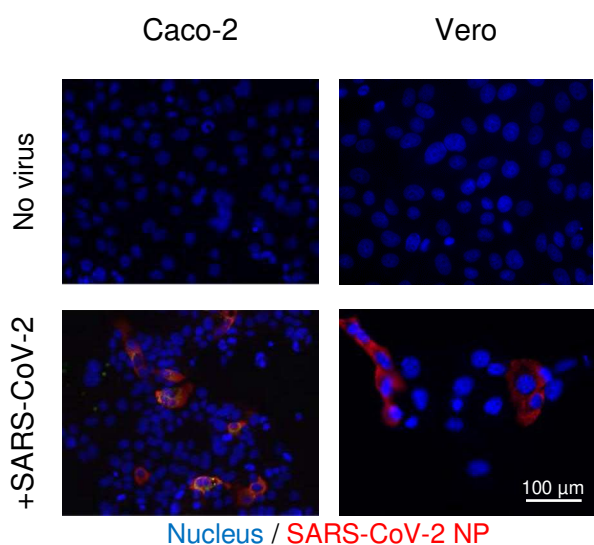
B



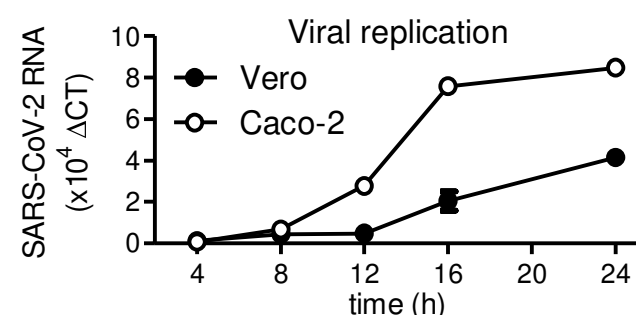
E



C



F



G

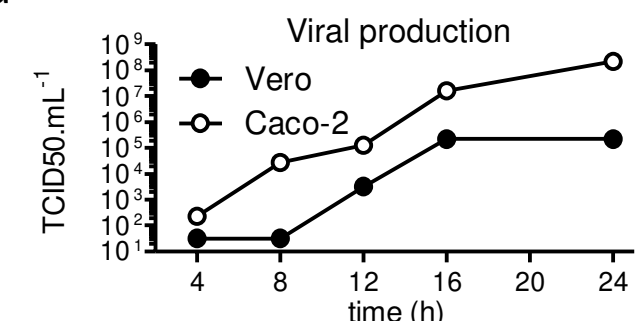
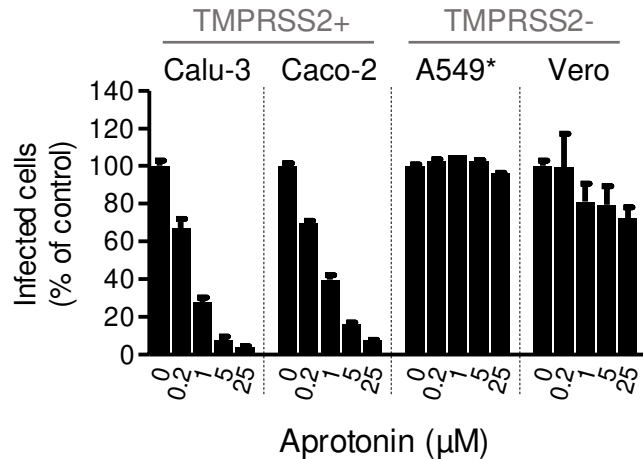
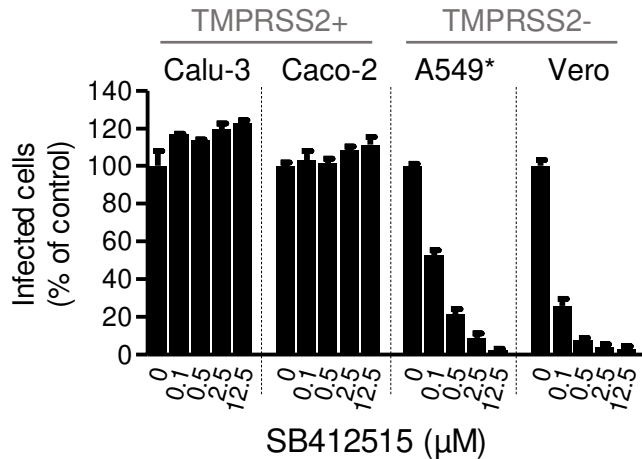


Fig. 1

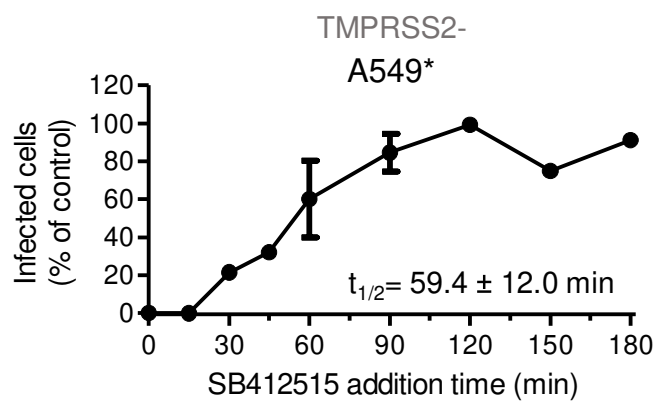
A



B

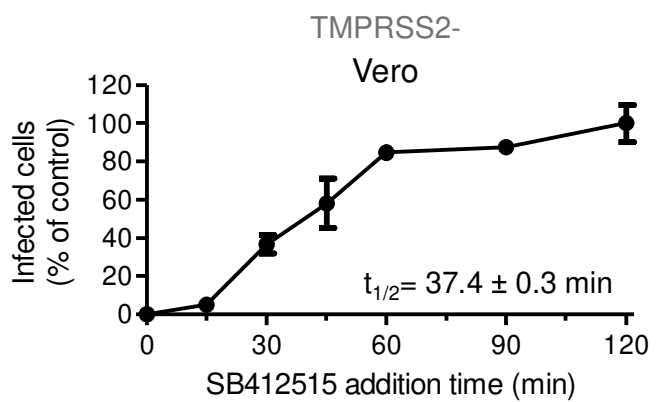


C

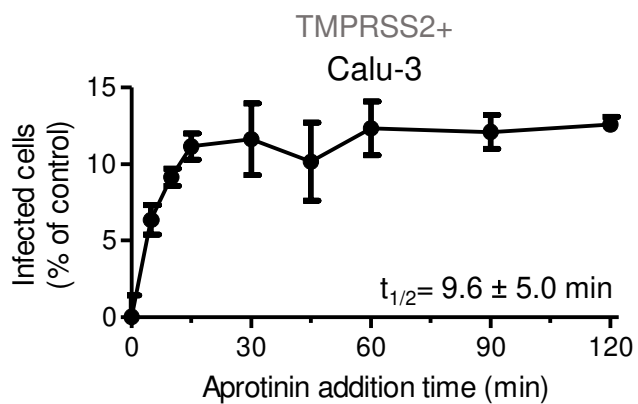


TMPRSS2-

Vero



D



TMPRSS2+

Caco-2

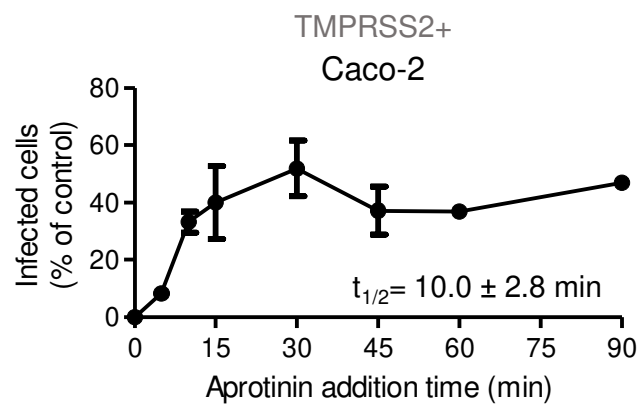


Fig. 2

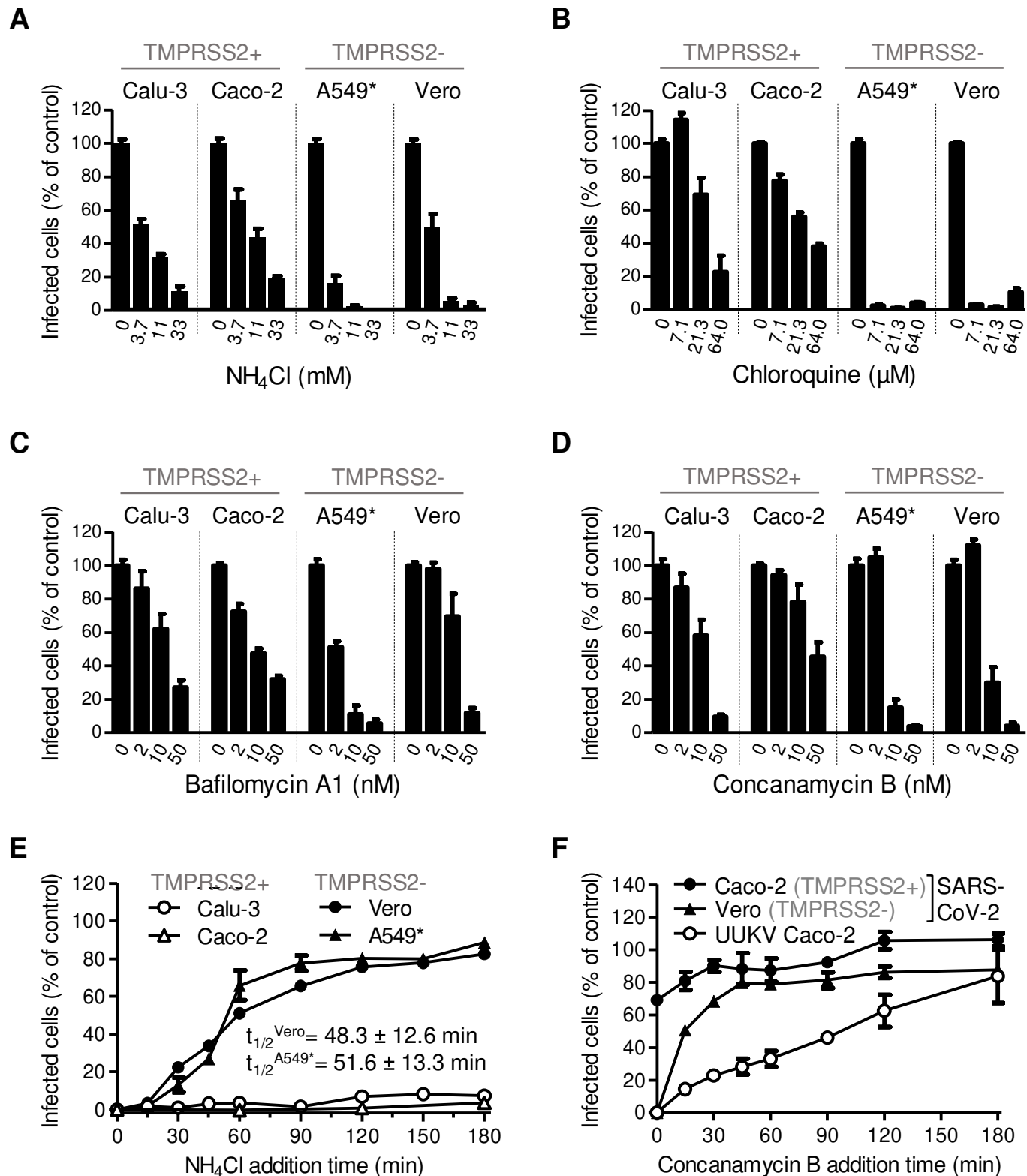


Fig. 3

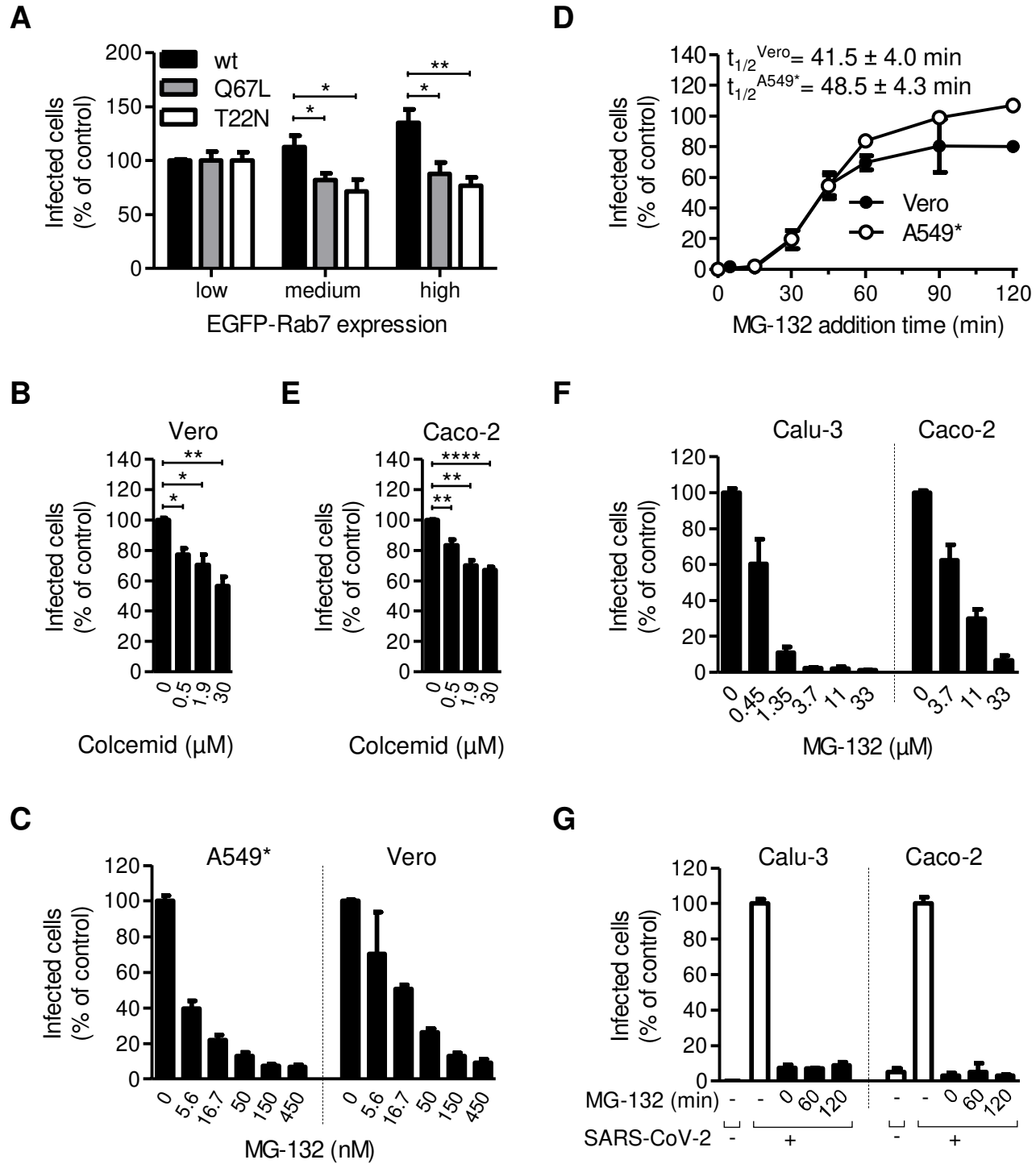


Fig. 4

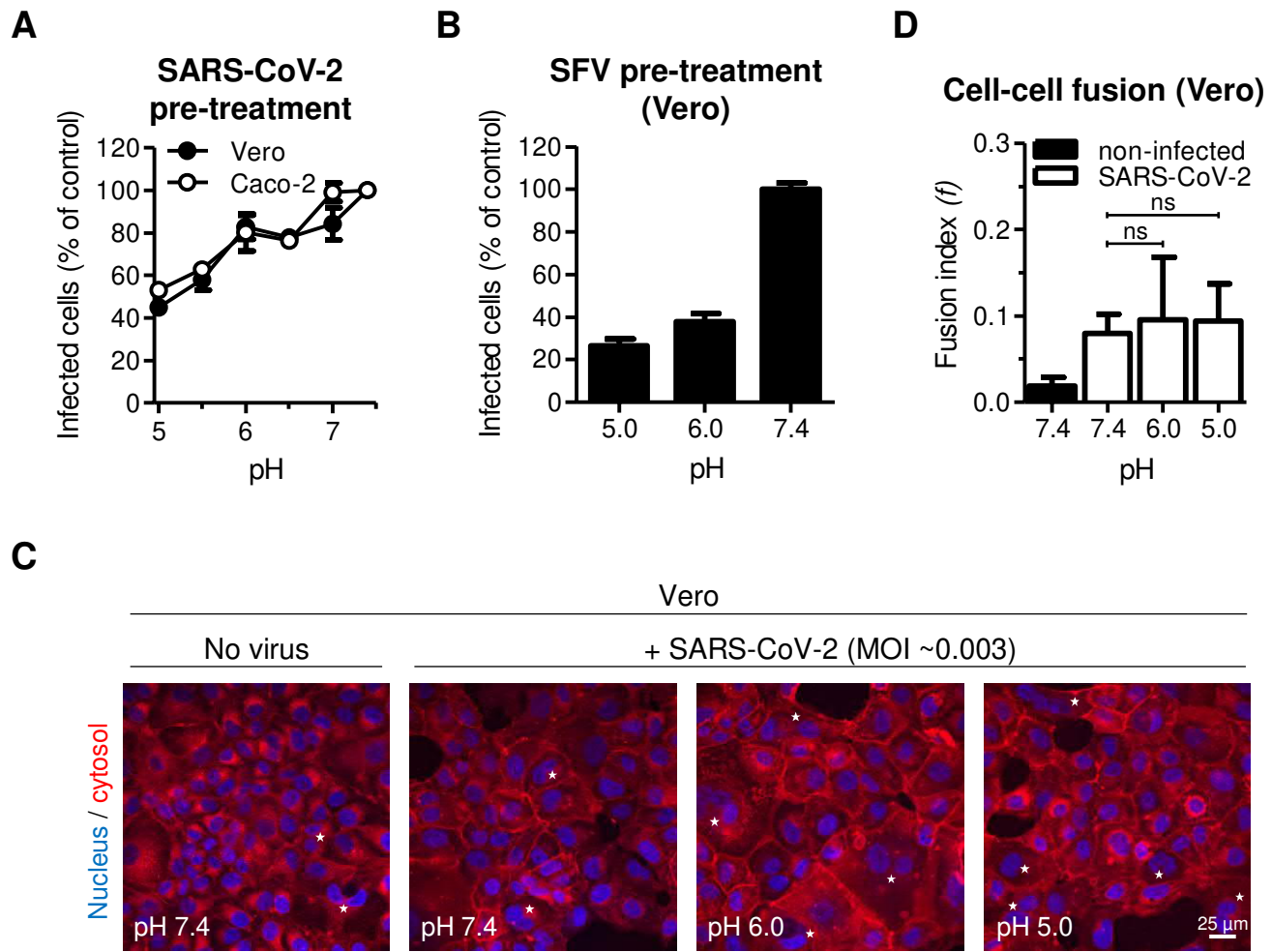


Fig. 5

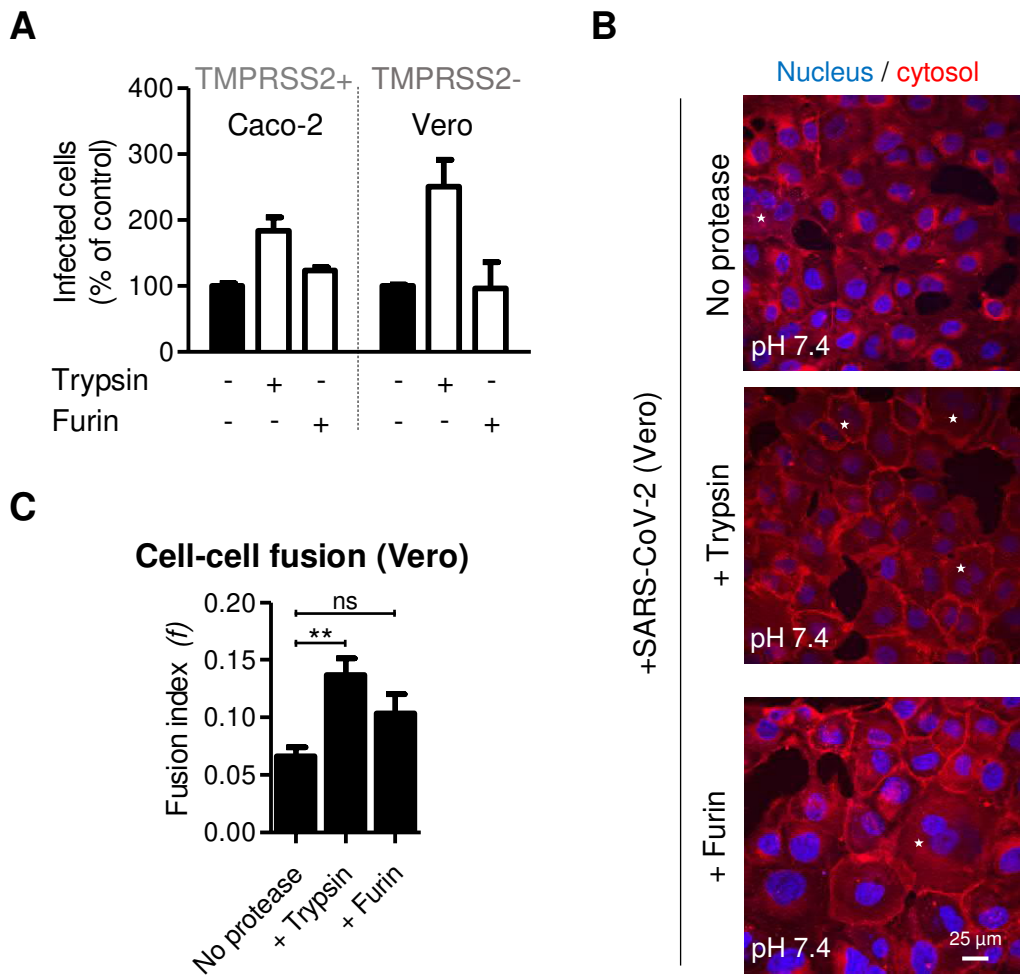


Fig. 6

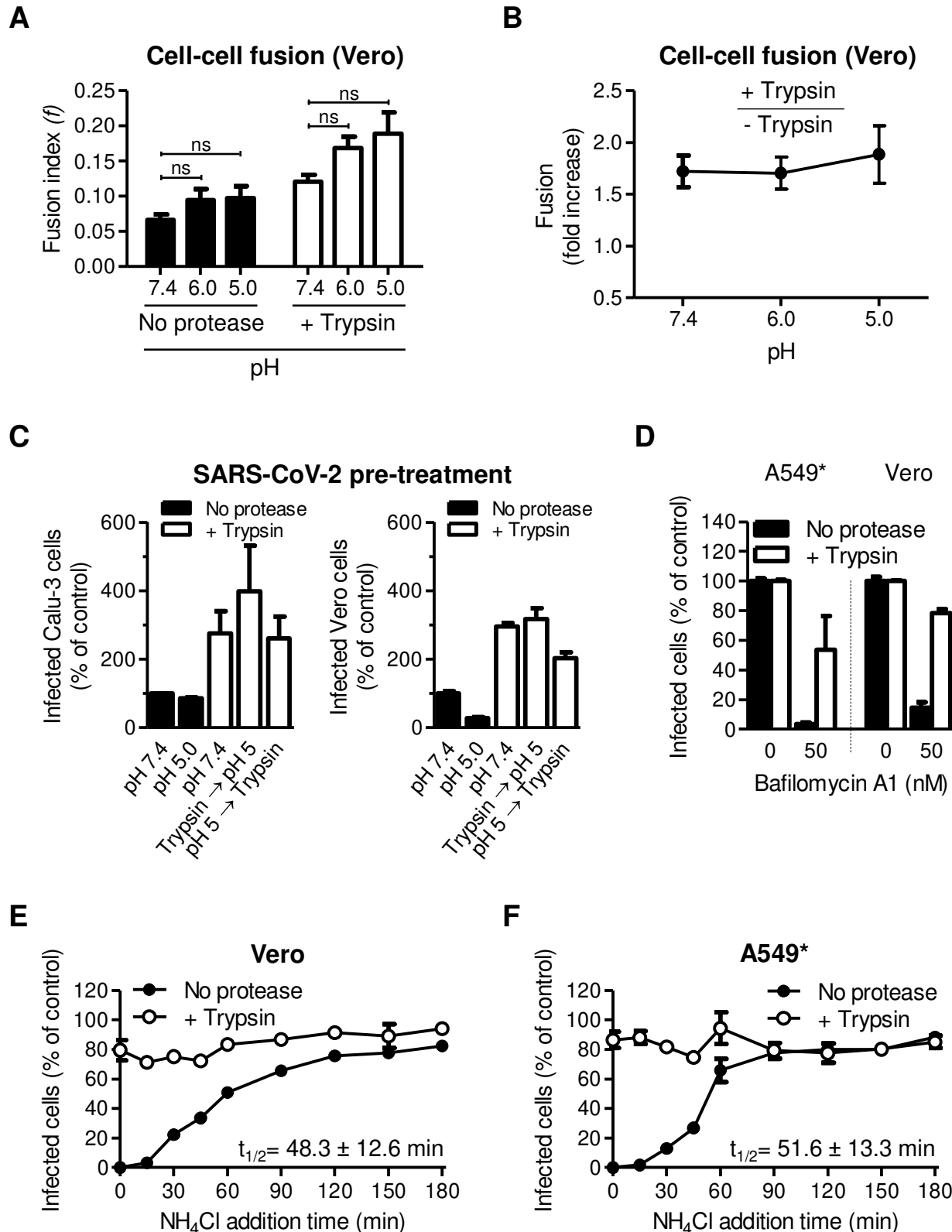


Fig. 7

| | Calu-3 | Caco-2 | A549* | Vero |
|--------------------|----------------|----------------|-----------------|----------------|
| Aprotonin | 0.4 ± 0.1 µM | 0.6 ± 0.0 µM | x | x |
| SB412515 | x | x | 125.7 ± 29.9 nM | 36.9 ± 10.9 nM |
| NH ₄ Cl | 4.4 ± 0.9 mM | 7.9 ± 2.4 mM | 2.2 ± 0.1 mM | 2.5 ± 0.6 mM |
| Chloroquine | 50.1 ± 24.4 µM | 27.4 ± 4.0 µM | 0.3 ± 0.0 µM | 0.2 ± 0.1 µM |
| Bafilomycin A1 | 16.3 ± 6.6 nM | 10.4 ± 3.2 nM | 2.0 ± 0.6 nM | 18.6 ± 7.7 nM |
| Concanamycin B | 12.2 ± 5.8 nM | 50.3 ± 30.4 nM | 6.0 ± 1.2 nM | 8.6 ± 2.2 nM |
| MG-132 | 0.7 ± 0.2 µM | 5.2 ± 2.1 µM | 4.4 ± 1.4 nM | 16.4 ± 5.6 nM |

Table 1